UNIVERSIDADE ESTADUAL DE CAMPINAS
FACULDADE DE ENGENHARIA MECÂNICA E INSTITUTO DE GEOCIÊNCIAS

ESHAIL MIGUEL VALLEJOS MELENDRES

Study of Friction Factor in Single-Phase Flow of Viscoplastic Fluid in Pipes

Estudo de Fator de Fricção em Escoamentos Monofásicos de Fluido Viscoplástico em Tubos

Campinas

2024

ESHAIL MIGUEL VALLEJOS MELENDRES

Study of Friction Factor in Single-Phase Flow of Viscoplastic Fluid in Pipes

Estudo de Fator de Fricção em Escoamentos Monofásicos de Fluido Viscoplástico em Tubos

Dissertation presented to the School of Mechanical Engineering and Institute of Geosciences of the University of Campinas in partial fulfillment of the requirements for the degree of Master in Sciences and Petroleum Engineering, in the Area of Exploitation.

Dissertação apresentada à Faculdade de Engenharia Mecânica e Instituto de Geociências da Universidade Estadual de Campinas como parte dos requisitos exigidos para a obtenção do título de Mestre em Ciências e Engenharia de Petróleo, na Área de Explotação.

Orientador: Prof. Dr. Marcelo Souza de Castro

Coorientadora: Dra. Daiane Mieko Iceri

ESTE TRABALHO CORRESPONDE À VERSÃO FINAL DA DISSERTAÇÃO DE MESTRADO ACADÊMICO DEFENDIDA PELO ALUNO ESHAIL MIGUEL VALLEJOS MELENDRES, E ORIENTADA PELO PROF. DR. MARCELO SOUZA DE CASTRO.

Campinas

2024

Ficha catalográfica
Universidade Estadual de Campinas (UNICAMP)
Biblioteca da Área de Engenharia e Arquitetura
Rose Meire da Silva - CRB 8/5974

V242s

Vallejos Melendres, Eshail Miguel, 1996-
Study of friction factor in sigle-phase flow of viscoplastic fluid in pipes / Eshail Miguel Vallejos Melendres. – Campinas, SP : [s.n.], 2024.

Orientador: Marcelo Souza de Castro.
Coorientador: Daiane Mieko Iceri.
Dissertação (mestrado) – Universidade Estadual de Campinas (UNICAMP), Faculdade de Engenharia Mecânica.

1. Fluidos não-newtonianos. 2. Fluxo laminar. 3. Fricção. 4. Número de Reynolds. 5. Pressão - Medição. 6. Carbopol. I. Castro, Marcelo Souza de, 1986-. II. Iceri, Daiane Mieko. III. Universidade Estadual de Campinas (UNICAMP). Faculdade de Engenharia Mecânica. IV. Título.

Informações Complementares

Título em outro idioma: Estudo de fator de fricção em escoamentos monofásicos de fluido viscoplástico em tubos
Palavras-chave em inglês:
Non-Newtonian fluids
Laminar flow
Friction
Reynolds number
Pressure - Measurement
Carbopol
Área de concentração: Explotação
Titulação: Mestre em Ciências e Engenharia de Petróleo
Banca examinadora:
Daiane Mieko Iceri [Coorientador]
Valdir Estevam
Francisco Júlio do Nascimento
Data de defesa: 26-07-2024
Programa de Pós-Graduação: Ciências e Engenharia de Petróleo

Identificação e informações acadêmicas do(a) aluno(a)
- ORCID do autor: https://orcid.org/0009-0002-0815-3119
- Currículo Lattes do autor: https://lattes.cnpq.br/4510751561152355

UNIVERSIDADE ESTADUAL DE CAMPINAS

FACULDADE DE ENGENHARIA MECÂNICA E INSTITUTO DE GEOCIÊNCIAS

DISSERTAÇÃO DE MESTRADO ACADÊMICO

Study of Friction Factor in Single-Phase Flow of Viscoplastic Fluid in Pipes Estudo de Fator de

Fricção em Escoamentos Monofásicos de Fluido Viscoplástico em Tubos

Autor: Eshail Miguel Vallejos Melendres

Orientador: Prof. Dr. Marcelo Souza de Castro
Coorientador: Dra. Daiane Mieko Iceri

A Banca Examinadora composta pelos membros abaixo aprovou esta Dissertação de Mestrado Acadêmico:

Dra. Daiane Mieko Iceri, Presidente
Center for Energy and Petroleum Studies (CEPETRO)
Universidade Estadual de Campinas (UNICAMP)

Prof. Dr. Valdir Estevam
Faculdade de Engenharia Mecânica
Universidade Estadual de Campinas (UNICAMP)

Prof. Dr. Francisco Júlio do Nascimento
Instituto do Mar
Universidade Federal de São Paulo (UNIFESP)

A Ata de Defesa com as respectivas assinaturas dos membros encontra-se no SIGA/Sistema de Fluxo de Dissertação/Tese e na Secretaria do Programa da Unidade.

Campinas, 26 de julho 2024

DEDICATORY

I dedicate this effort to my parents, Miguel and Judith, and to my siblings, Cristian Paolo and Evani Camiri, for their unwavering emotional and financial support in all my personal and professional projects, regardless of the distance.

To my great-grandfather José (†) and my grandfather Emiliano (†), who bequeathed the noble oil tradition to my father and me.

To myself, for having achieved this milestone despite the gray hairs, and for having found a new passion in fluid mechanics.

And, above all, to God, with whom I speak every day and who has never let me feel His absence. I know He intercedes through my family and friends and has always guided me to make the right decisions that have brought me to this point.

ACKNOWLEDGEMENTS

I would like to thank my parents from the bottom of my heart for always providing my siblings and me with the emotional motivation and necessary means to excel academically. Their constant encouragement to keep improving has allowed me to get this far, and I will be eternally grateful to them for that. I extend my gratitude to my uncle Hernan "Chacho" Vallejos for his unwavering support in my times of need.

Words fail to fully express the depth of my gratitude to Prof. Dr. Marcelo and Dra. Daiane for their trust and support, which allowed me to join the ALFA research group in the Plug-In project at one of the most crucial moments of my academic journey. Prof. Marcelo's always positive attitude and Daiane's dedication to our project have served as constant sources of motivation. I am truly honored to have worked under their guidance.

And, Daiane, I sincerely appreciate your willingness to help me overcome all the challenges that arose during this research. Because of you, I achieved the significant results of this work. My gratitude will always be directed towards you.

I cannot forget Msc. Kenji Matoba, who accompanied me to run of all the experimental tests. The laughs and our mutual passion for mathematics will never be forgotten.

To José Maria H., Juan T., Marx M., Walter F., Andrey C., André P., Julia V., Malu R., Adriel N., Carlos N., Andrique D., and of course, to my friends from the ALFA and the Pandêmicos group, and my homemates for the activities within and outside the academic field.

I also thank the Artificial Lift and Flow Assurance (ALFA) group and the Center for Energy and Petroleum Studies (CEPETRO) at UNICAMP for providing me the necessary resources to undertake this research. Furthermore, a special thanks to the technicians Cláudio Varani, Luís Gustavo da Silva, and Edmilson Sanches Silva.

My studies were funded by the *Programa de Formação de Recursos Humanos* (PRH-5-ANP) of the *Agência Nacional do Petróleo, Gás Natural e Biocombustíveis* (ANP), and later by the *Coordenação de Aperfeiçoamento de Pessoal de Nível Superior – Brasil* (CAPES) - Finance Code 001.

TotalEnergies Brasil funded the experimental infrastructure under the operation contract TEPBr/RD21-73 as part of the project "A fundamental research on the stratified two-phase flow of a gas and a viscoplastic fluid in pipes".

“Math is the language which God has written the Universe”.

Galileu Galilei

“Your objective should be to win. To win, win, win all the time. Not sometimes, every time”.

Sumner Murray Redstone in The Men Who Built America (S1, E1)

RESUMO

Dimensionar tiebacks submarinos para o transporte de petróleo parafínico em ambientes, onde as condições de temperatura podem ser inferiores à temperatura de aparecimento de cristais de parafinas (WAT), podem apresentar desafios adicionais, como prever a queda de pressão no sistema torna-se um desafio devido à mudança no comportamento reológico do fluido transportado. O modelo de Herschel-Bulkley pode descrever o comportamento da viscosidade do petróleo com características viscoplásticas. Modelos disponíveis na literatura para o cálculo do número de Reynolds e do fator de atrito em regime laminar para fluidos Herschel-Bulkley apresentam ainda algumas divergências. O presente estudo buscou avaliar experimentalmente a capacidade dessas equações para prever a queda de pressão, utilizando uma solução aquosa de Carbopol 940 e Trietanolamina que reproduz o comportamento ideal de um fluido com características viscoplásticas. Os experimentos foram realizados em um aparato experimental com diâmetro interno de 0.0539 m, comprimento de desenvolvimento de fluxo de 20 m e uma seção de teste de 2.4 m. Nos resultados, as combinações de fator de atrito e número de Reynolds recomendadas na literatura mostraram um desvio médio superior a $10\,\%$ em relação aos dados experimentais deste trabalho. Dessa forma, uma análise combinatória entre os diferentes modelos de número de Reynolds e fator de atrito foi realizada para avaliar se uma possível combinação alternativa seria mais eficiente em capturar os resultados de maneira mais consistentes. Baseado nos dados experimentais deste estudo e validado com dados coletados da literatura em que utilizaram soluções de Carbopol 940 e 980, concluiu-se que para fluidos Herschel-Bulkley a combinação do fator de atrito para fluidos newtonianos em regime laminar e o número de Reynolds de Slatter preveem a queda de pressão com uma aproximação entre $5.3\,\%$ e $12.0\,\%$ em relação aos valores medidos. Além disso, a equação de queda de pressão para fluidos Power Law de Metzner e Reed teve uma aproximação de até $13.8\,\%$ em relação aos dados experimentais. As conclusões deste trabalho são relevantes, pois reforça a limitada literatura disponível sobre o escoamento interno de fluidos Herschel-Bulkley em tubulações.

Palavras–chave: Herschel-Bulkley, Fluido viscoplástico, Fator de atrito de Fanning, Número de Reynolds, Carbopol.

ABSTRACT

Designing submarine tiebacks for transporting waxy crude oil in environments where temperature conditions can be below the Wax Appearance Temperature (WAT) may pose additional challenges. Predicting pressure drop in the system becomes challenging due to the change in rheological behavior of the transported fluid. The Herschel-Bulkley model can describe the viscosity behavior of oil with viscoplastic characteristics. Models available in the literature for calculating Reynolds number and friction factor in laminar flow for Herschel-Bulkley fluids still exhibit some divergences. This study aimed to experimentally evaluate the capability of these equations to predict pressure drop, using an aqueous solution of Carbopol 940 and Triethanolamine to simulate the ideal behavior of a fluid with viscoplastic characteristics. Experiments were conducted in an experimental apparatus with an internal diameter of 0.0539 m, a flow development length of 20 m, and a test section of 2.4 m. In the results, combinations of friction factor and Reynolds number recommended in the literature showed an average deviation greater than $10\,\%$ compared to the experimental data of this study. Thus, a combinatorial analysis using different models of Reynolds number and friction factor was performed to assess if an alternative combination could more efficiently capture results consistently. Based on the experimental data from this study and validated with data collected from the literature using Carbopol 940 and 980 fluids, it was concluded that for Herschel-Bulkley fluids, the combination of friction factor for Newtonian fluids in the laminar regime and the Reynolds number of Slatter predicts pressure drop with an approximation between $5.3\,\%$ and $12.0\,\%$ relative to the measured values. Additionally, the pressure drop equation for Power Law fluids by Metzner and Reed showed an approximation of up to $13.8\,\%$ compared to experimental data. The conclusions of this study are relevant as they reinforce the limited available literature about the internal flow of Herschel-Bulkley fluids in pipelines.

Keywords: Herschel-Bulkley, Viscoplastic fluid, Fanning friction factor, Reynolds Numbers, Carbopol.

LIST OF FIGURES

LIST OF TABLES

LIST OF ABBREVIATIONS AND ACRONYMS

API	American Petroleum Institute
B	Bingham plastic fluid
CEPETRO	Center for Energy and Petroleum Studies
DPL	Dual Power Law
DSR	Dimensionless Shear Rate
GSS	Golden Section Search
CF	Curve fitting
LabPetro	Petroleum Experimental Laboratory
MAE	Mean absolute error
MAPE	Mean absolute percentage error
PL	Power Law fluid
Rpm	Revolutions per minute
TEA	Triethanolamine
UNICAMP	Universidade Estadual de Campinas
WAT	Wax appearance temperature

LIST OF SYMBOLS

A	Area (m^2)
D	Pipe diameter (m)
f	Fanning friction factor $(-)$
f_D	Darcy friction factor $(-)$
K'	Derivative of consistency index of Metzner and Reed $(Pa.s^n)$
k	Consistency index $(Pa.s^n)$
L	Pipe length (m)
$\dot{m}_l$	Liquid mass flow (kg/h)
m	Total number of observations $(-)$
n	Power Law index $(-)$
N_{Re}	Reynolds number $(-)$
$N_{\text{Re, Metzner}}$	Reynolds number of Metzner and Reed $(-)$
$N_{\text{Re, Slatter}}$	Reynolds number of Slatter $(-)$
$N_{\text{Re, Güzel}}$	Reynolds number of Güzel $(-)$
$N_{\text{Re, Madlener}}$	Reynolds number of Madlener $(-)$
P	Absolute pressure (Pa)
Q	Flow rate (m^3/s)
R	Pipe radius (m)
T	Temperature $(^\circ C)$
$\bar{V}$	Mean flow velocity (m/s)

V_z	Velocity in the annular space between the plug flow region and the pipe wall (m/s)
V_{zp}	Velocity in the plug flow region (m/s)
y_i	Measured or true data
$\hat{y}_i$	Predicted data

GREEK SYMBOLS

ϵ	Roughness (m)
η	Apparent viscosity $(Pa.s)$
η_∞	Constant viscosity in the very high shear rate range $(Pa.s)$
μ	Dynamic viscosity $(Pa.s)$
ϕ	Relationship between the radius of the plug and the radius of the pipe, R_p/R
ρ	Fluid density (kg/m^3)
τ_{yx}	Shear stress (Pa)
τ_w	Shear stress at wall (Pa)
τ_0	Yield stress for any type of fluid (Pa)
τ_0^B	Yield stress for Bingham Plastic fluids (Pa)
τ_0^H	Yield stress for Herschel-Bulkley fluids (Pa)
$\dot{\gamma}_{yx}$	Shear rate $(1/s)$

CONTENTS

1 INTRODUCTION

The exploration of petroleum basins in deep and ultra-deep waters, situated under adverse environmental conditions, represents a significant challenge for flow assurance due to the presence of waxy crude oils (Dalla *et al.*, 2019). This obstacle has become increasingly prevalent in discoveries in Brazil, where waxy crude oil constitutes a significant portion of reserves, as in the current scenarios of the Campos and Recôncavo basins (Rocha *et al.*, 2003; Oliveira *et al.*, 2012).

As an alternative for transporting hot crude oil from these basins to onshore installations, facilities such as subsea tiebacks have been employed, offering a low-cost solution, especially effective for deep waters and long distances conditions. However, these conditions also represent a challenge in terms of oil production due to the temperature difference between the water surrounding the pipeline and the transported fluid, inducing heat transfer from the crude oil to the marine environment, resulting in the deposition of paraffins. This progressive cooling changes drastically the kinematic viscosity of the crude oil and increases the surface resistance to flow of the transported fluid, leading to a change in the flow regime from turbulent to laminar (Rønningsen, 1992; Swamee, 1993).

Therefore, the challenge is not limited solely to the reduction of the internal diameter of the tieback due to paraffin deposition, but it is also associated with the ability to predict pressure drops due to the change in fluid behavior. During transport process, in environments where the temperature can drop to levels considerably lower than the typical Wax Appearance Temperature (WAT), crude oils, which normally exhibits Newtonian behavior, undergo a transition to non-Newtonian behavior. In this new state, the crude may display rheological characteristics such as shear-thinning fluids and may even exhibit time-dependent properties. This change is attributed to the formation of wax crystals and the creation of a cross-linked structural network, similar to polymer gels with yield stress (Dalla *et al.*, 2019).

According to Rønningsen (1992) and Bao e Zhang (2020), the rheological model that best describes the flow curve behavior of gelled crude oil is the Herschel-Bulkley (also known as viscoplatic or yield-pseudoplastic) model. This model states that the fluid behaves as a rigid solid when the applied external stress is less than the fluid's yield stress (τ_0^H) and as a viscous liquid when the applied stress exceeds this limit.

The model fluid used to replicate the Herschel-Bulkley behavior of gelled crude oils is composed by Carbopol® and Triethanolamine. Curran *et al.* (2002) pointed out that Carbopol polymer is highly appreciated in the research community because of its behavior resembling that of an idealized yield stress fluid and because it was employed by different authors to replicate the waxy crude oil behavior (e.g. Taghavi *et al.* (2012), Alba *et al.* (2013), Sierra *et al.* (2016), Liu e Bruyn (2018)). Triethanolamine was added to the solution to improve its viscosity. According to the study by Iceri *et al.* (2023), acts as a pH neutralizer, viscosifier, and prevents fungal formation in the solution.

1.1 Motivation

After reviewing the relevant literature on Herschel-Bulkley fluids, covering studies conducted over the last 70 years, it was noted that there is disagreement over a common model that can reliably forecast the pressure drop resulting from the transport of viscoplastic fluids in circular-section pipe systems. This is explained by the fact that models like the Bingham plastic or Power Law are typically used to describe non-Newtonian fluids.

In spite of various proposals on this field, research has focused mainly on the analysis of the behavior of these viscoplastic fluids in concentric and eccentric annular spaces, primarily motivated by the need to understand the fluids used in oil well drilling. Several authors (e. g. Hanks (1979), Fordham *et al.* (1991), Founargiotakis *et al.* (2008), Kelessidis *et al.* (2011), Qi *et al.* (2013), among others), have contributed to this area by proposing theories on flow in concentric geometries, friction factor-independent methodologies to calculate pressure drop, among others. In relation to research on internal flow of viscoplastic fluids, the proposed equations are more limited and often derived analytically. Their validation has been limited to comparisons with numerical results or comparisons between different models, and in several cases could not be experimentally tested.

Despite theoretical and numerical validations between different models yielding results with up to a 10% difference, some conclusions were drawn, such as the laminar flow characterization for non-Newtonian fluids is fully understood (Kelessidis *et al.*, 2011), and the truth is that these fluids cannot be described by a single model. For example, Chilton e Stainsby (1998) indicated that these solutions are not really applicable to all non-Newtonian fluids, while Founargiotakis *et al.* (2008) and Qi *et al.* (2013) added that, without considering numerical solutions, traditional methodologies for predicting pressure drop in annular laminar flow have

limited accuracy.

In summary, despite annular flow being the most studied scenario regarding Herschel-Bulkley fluids, there is still no precise methodology to predict pressure drop. On the other hand, as far as our specific problem is concerned, although the internal flow for Herschel-Bulkley fluids is geometrically simpler, it is not necessarily a more favorable working scenario due to the limited literature available, as will be demonstrated in the Literature Review section.

1.2 Objective

The research work aims to investigate the friction factor in single-phase flow of a viscoplastic fluid in pipes.

The general objective of this project will be achieved by following the specific objectives:

- Evaluate the behavior of the friction factor of a viscoplastic fluid using experimental pressure drop data.
- Compare the results of the friction factor correlations and their recommended Reynolds number models with the experimental friction factor data obtained to assess their accuracy in calculating the pressure drop.
- Perform a combinatorial analysis to examine alternative combinations of Reynolds number models and friction factor correlations in order to approximate the analytical results to the experimental data.
- Validate the best combinations of Reynolds number models and friction factor correlations found in this study using available literature data to demonstrate their applicability and consistency in predicting the pressure drop.

2 FUNDAMENTAL CONCEPTS

This chapter presents the fundamental concepts that underpin the theoretical basis of this research. The classification and rheological models that describe the behavior of different types of fluids when subjected to stresses or strains, primarily focusing on the theory of viscoplastic fluids are discussed. Additionally, the rheological properties characteristic of each fluid type are detailed, along with a description of how these properties influence their behavior.

2.1 Newtonian fluids

Newtonian fluids are characterized by a constant viscosity, which remains unchanged under stress. It follows the Newton's law of viscosity, which states that the stress experienced by a fluid is proportional to its rate of deformation or shear rate. Water, air, and the most liquid metals are classic examples of Newtonian fluids. Their viscosity does not change with the strain rate or velocity of the fluid, but only with changes in pressure and temperature.

The Newton's Law of viscosity applies to any gas or liquid in a laminar flow and a molecular weight less than 5000 g/mol. Figure 2.1 shows a schematic representation to derived the Equation 2.1. This system of parallel plates of surface area A contains fluid between them and are separated by a distance $\mathrm{d}y$. Over time, the upper plate will move at a constant velocity $\mathrm{d}V_x$, generating momentum in the fluid and forming a linear steady-state velocity profile between the plates. To keep the upper plate moving, the application of a constant force F is required (Bird *et al.*, 2006). Furthermore, the law assumes that the acceleration in the flow between plates is zero, the pressure in the flow direction is constant and there is no slip at the surfaces of both plates (White, 2018). The equation for calculating the Newton's viscosity is given by Equation 2.1:

$$\frac{F}{A} = \mu \left(-\frac{\mathrm{d}V_x}{\mathrm{d}y} \right) \tag{2.1}$$

where viscosity is represented by μ. The relation $(-\mathrm{d}V_x/\mathrm{d}y)$ represents the shear rate, commonly denoted as $\dot{\gamma}_{yx}$. It refers to the measure of the velocity of deformation experienced by a fluid in response to an applied shear force. In other words, it can be formulated as the velocity gradient perpendicular to the direction of the applied shear stress. The parameter (F/A) represents shear stress, this is the force per unit area required to move the fluid and can also be expressed as τ_{yx}. Therefore, Equation 2.1 can be rearranged as Equation 2.2. For both τ_{yx} and

$\dot{\gamma}_{yx}$, the initial subscript (y) specifies the direction that is perpendicular to the shearing plane. Meanwhile, the latter subscript (x) designates the direction in which the force is applied and the flow occurs (Chhabra; Richardson, 2011).

$$\tau_{yx} = \mu \dot{\gamma}_{yx}. \tag{2.2}$$

Figure 2.1 – Fluid flow between parallel plates (Chhabra; Richardson, 2011).

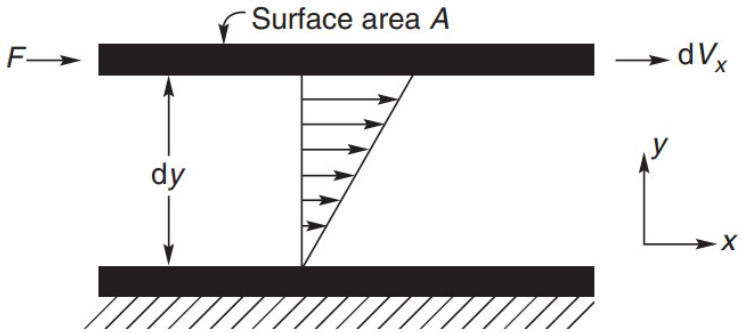

2.2 Non-Newtonian fluids

A non-Newtonian fluid is characterized by its flow curve (shear stress vs. shear rate), which is not necessarily linear and, in some cases, may not pass through the origin. This behavior is attributed to the high molecular weight of the molecules that make up the fluid. Consequently, the apparent viscosity of the fluid does not remain constant under conditions of constant pressure and temperature, and it is significantly influenced by the velocity gradient, flow geometry, etc. This behavior contrasts with what is observed in Newtonian fluids (Bird *et al.*, 2006; Chhabra; Richardson, 2011).

Conveniently, the non-Newtonian fluids can be grouped into three general classes: Time-independent fluids (also known as: inelastic, purely viscous, or generalized Newtonian fluids, GNF), Time-dependent fluids, and Viscoelastic fluids.

This study will focus on detailing fluids with time-independent properties, as viscoplastic fluids fall into this category.

2.2.1 Time-independent fluids

These fluids are known for their rheological properties that do not change over time. This class of material follows a mathematical model, described by Equation 2.3, which depicts the relationship between the strain rate and shear stress. This relationship is expressed as:

$$\dot{\gamma}_{yx} = f(\tau_{yx}) \tag{2.3}$$

or its inverse form,

$$\tau_{yx} = f(\dot{\gamma}_{yx}). \tag{2.4}$$

This implies that for any value of $\dot{\gamma}_{yx}$ at any point it is uniquely determined by a value of τ_{yx} or vice versa.

Depending on the shape of the flow curve formed by these two parameters, as is shown in Figure 2.2, fluids may be further subdivided into three types, as described in the following:

Figure 2.2 – Newtonian and non-Newtonian fluid flow curves (Chhabra; Richardson, 2011).

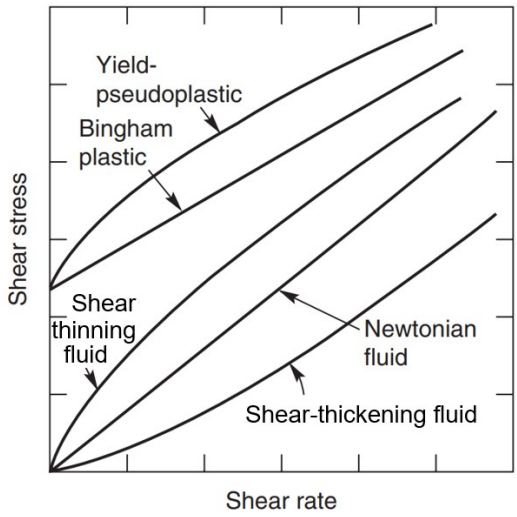

2.2.1.1 Shear-thinning or pseudoplastic fluids

Most non-Newtonian fluids (i.e. polymer solutions, colloidal suspensions) can be classified in this group, also called pseudoplastic fluids. It is characterized by the inverse relationship between the apparent viscosity and shear rate. While shear rate increases, apparent viscosity decreases.

To model the rheological behavior of shear-thinning fluids, mathematical expressions, either empirical or based on kinetic theory applied to the liquid state, have been proposed to fit the curve of rheological data that relates the shear rate to shear stress.

i) Power-law model

The empirical Power Law equation is the most classic model used to explain the rheological characteristics of pseudoplastic fluids (Ostwald; Auerbach, 1926) which relates the share stress to the share rate with a power called: flow behavior index or Power Law index (n).

Saramito (2016) cited that the model formulated in Equation 2.5 offers a partial explanation about non-Newtonian fluid behavior. According to his description, when the Power

Law index is less than 1, the effective viscosity would decrease to nearly zero as the shear rate becomes very large. However, due to the physics and chemistry at the molecular scale of fluids, liquids display a minimum and maximum effective viscosity.

The Power Law model is given by the expression:

$$\tau_{yx} = k(\dot{\gamma}_{yx})^n. \tag{2.5}$$

This equation, plotted in Cartesian coordinate systems, graphs a flow curve that can have a positive or negative shape depending on the value of the flow behavior index (n), as shown in Figure 2.3:

Figure 2.3 – Power Law index (Tropea *et al.*, 2007).

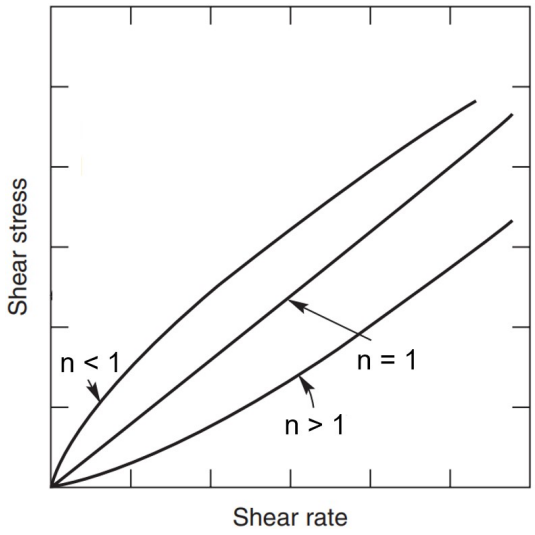

The dimensionless Power Law index (n) describes the degree of non-Newtonian behavior of the fluid and characterizes the degree of shear-thinning or shear-thickening behavior. A value of $n < 1$ indicates that the fluid has shear-thinning behavior, meaning that its apparent viscosity (η) decreases as the shear rate increases. A value of $n > 1$ indicates that the fluid has shear-thickening behavior, meaning that its apparent viscosity increases as the shear rate increases. When $n = 1$, Equation 2.5 reduces to Equation 2.2, keeping the apparent viscosity constant and equal to the Newtonian viscosity $(\eta = \mu)$. Apparent viscosity is calculated following Equation 2.6. The consistency index k represents the resistance of the fluid to flow. A higher consistency index means the fluid is more resistant to flow and requires a greater force to initiate flow (Chhabra; Richardson, 2011).

$$\eta = \frac{\tau_{yx}}{\dot{\gamma}_{yx}} = \frac{k(\dot{\gamma}_{yx})^n}{\dot{\gamma}_{yx}} = k(\dot{\gamma}_{yx})^{n-1} \tag{2.6}$$

2.2.1.2 Viscoplastic fluids

Saramito (2016) describes viscoplastic fluids as materials capable of maintaining their original shape like a solid under the effects of gravity, yet able to flow like a liquid when it is subjected to sufficient stress to cause deformation. The minimum stress required to induce deformation is known as the yield stress (τ_0). According to Chhabra e Richardson (2011), the fluid deforms elastically as a solid body and behaves as a three-dimensional framework with sufficient stability to flow while keeping its shape when the externally applied stress is lower than the yields stress $(\tau_{yx} < \tau_0)$. But, once the yield stress is exceeded $(\tau_{yx} > \tau_0)$, the structure breaks down, and the substance exhibits characteristics of viscous fluid. If the flow curve of this fluid is plotted, it will exhibit a linear or nonlinear shape and, in any case, will not intersect the origin owing to the presence of τ_0, as shown in Figure 2.4, with the meat extract and Carbopol solution as the flowing examples:

Figure 2.4 – Shear stress–shear rate data illustrating the viscoplastic behavior of an Carbopol polymer solution (yield-pseudoplastic) and meat extract (Bingham plastic) (Chhabra; Richardson, 2011).

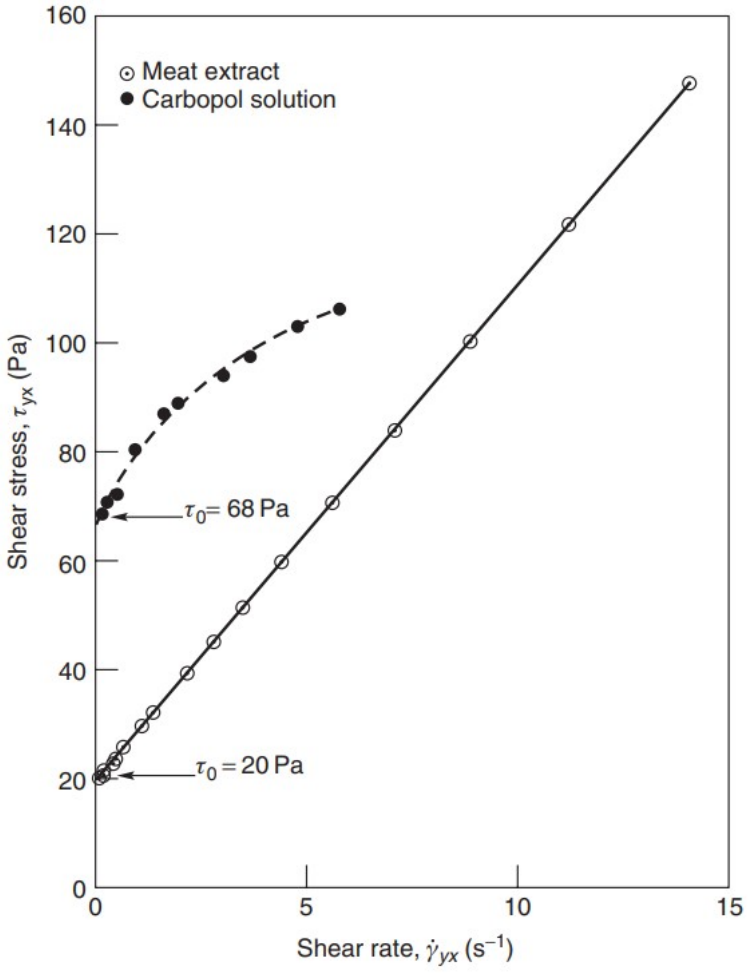

Two commonly used models for viscoplastic fluids are briefly described:

i) The Bingham plastic model

This model described by Equation 2.7 is characterized by a linear relationship between shear stress and shear rate once the minimum stress required for the liquid to start flowing, known as Bingham yield stress and denoted as τ_0^B, is exceeded:

$$\begin{array}{cc} \tau_{yx} = \tau_0^B + k(\dot{\gamma_{yx}}) & \text{for} \quad |\tau_{yx}| \geq \left|\tau_0^B\right| \\ \dot{\gamma}_{yx} = 0 & \quad\quad\;\; |\tau_{yx}| < \left|\tau_0^B\right| \end{array} \tag{2.7}$$

If Bingham yield stress is null, then the Bingham viscosity is constant $(k = \mu)$, and its equation reduces to Equation 2.2, the Newtonian fluid. The graphical representation of this behavior is shown in Figure 2.5:

Figure 2.5 – Bingham plastic fluid behavior (Chhabra; Richardson, 2011).

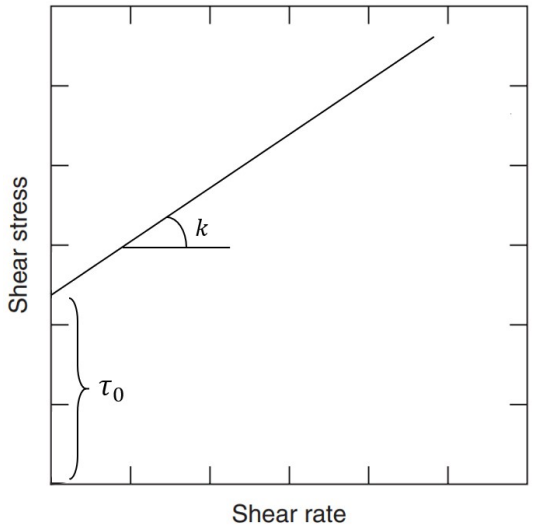

Apparent viscosity for Bingham fluids changes with the variation of shear stress and shear rate, as shown in Figure 2.6, and it is calculated following the relation of Equation 2.8

$$\eta = \frac{\tau_{yx_2} - \tau_{yx_1}}{\dot{\gamma}_{yx_2} - \dot{\gamma}_{yx_1}} \tag{2.8}$$

Figure 2.6 – Variation of apparent viscosity, η, for different shear stresses and shear rates for Bingham fluid (Created by the author).

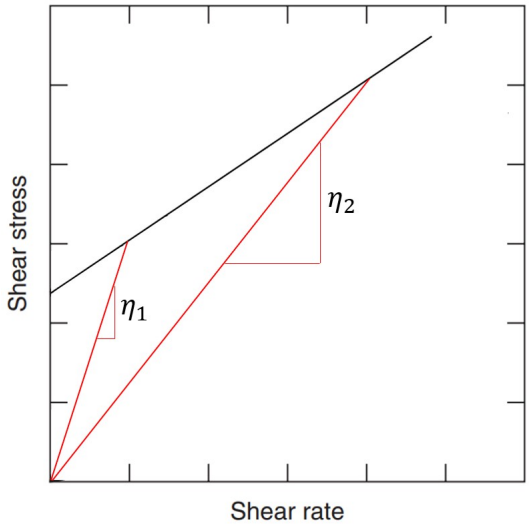

ii) The Herschel-Buckley fluid model

It is a generalization of the Bingham plastic model to improve the non-linear flow curve for shear stresses greater than the yield stress ($|\tau_{yx}| > |\tau_0^B|$), as shown in Figure 2.7:

Figure 2.7 – Herschel-Buckley fluid behavior for $n < 1$ (Chhabra; Richardson, 2011).

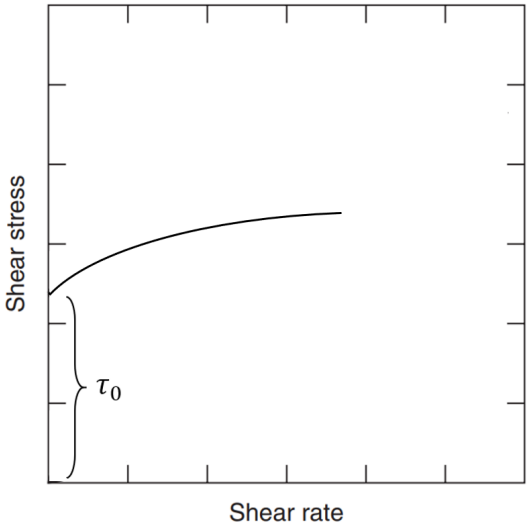

The behavior of the flow curve of this model is described by Equation 2.9,

$$\begin{array}{cc} \tau_{yx} = \tau_0^H + k(\dot{\gamma}_{yx})^n & \text{for} \quad |\tau_{yx}| \geq \left|\tau_0^H\right| \\ \dot{\gamma_{yx}} = 0 & \quad\quad\;\; |\tau_{yx}| < \left|\tau_0^H\right| \end{array} \tag{2.9}$$

where, τ_0^H is the Herschel-Buckley yield stress. The model assumes that the fluid behaves like a rigid solid below the τ_0^H and like a viscous liquid above it. The consistency index, denoted as

k, quantifies the resistance of a fluid to flow. The index n refers to the flow curve behavior or Power Law index, which indicates the shear-thinning characteristic of the fluid. This index can be determined experimentally by subjecting the fluid to different shear rates using a rheometer, an instrument used to measure rheological properties.

Note that if the Herschel-Buckley yield stress is reduced to 0 ($\tau_0^H = 0$), the fluid recovers the Power Law behavior, given by Equation 2.5. Additionally, if $k = \mu$ and $n = 1$, this model reduces to the Newtonian model given by Equation 2.2.

2.2.1.3 Shear-thickening or dilatant fluid behavior

Shear thickening is the tendency of some materials to have a higher viscosity when flowing at high shear rates. This behavior is exhibited by highly concentrated suspensions of small particles.

As long as the liquid lubricates the movement of each particle, there are low shear stresses at low shear rates. However, as the material expands at high shear rates, less liquid fills the void space and does not prevent solid-solid contact between particles, leading to greater friction and shear stresses. As shown in Figure 2.8 (Chhabra; Richardson, 2011):

Figure 2.8 – Schematic representation of shear-thickening behavior (Chhabra; Richardson, 2011).

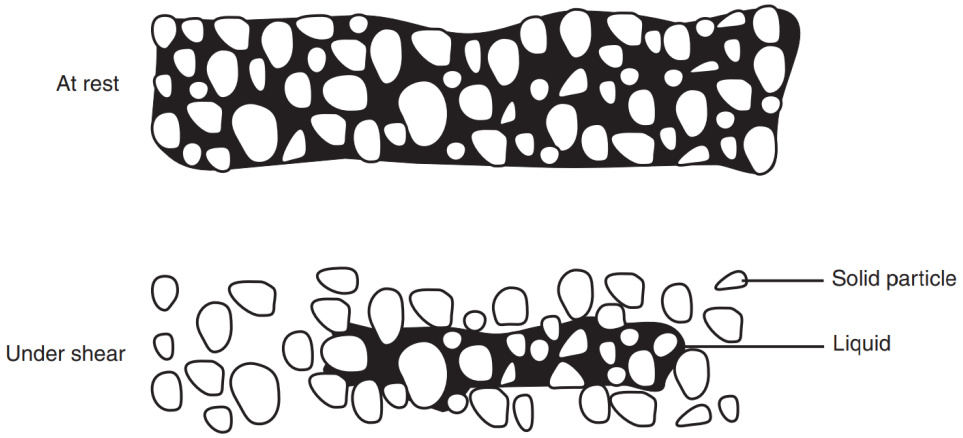

Figure 2.9 shows that the flow behavior of a dilatant fluid can describe by Power Law model (Equation 2.5) when n is greater than 1. Also, if n is higher than 1, the apparent viscosity η increases as the shear rate $\dot{\gamma}_{yx}$ increases and the relationship can be calculated with Equation 2.10,

$$\eta = \frac{\tau_{yx}}{\dot{\gamma}_{yx}} = k(\dot{\gamma}_{yx})^{n-1} = k\frac{(8V/D)^n}{\dot{\gamma}_{yx}}. \tag{2.10}$$

The parameter $8V/D$ can be correlated to the true shear rate by the Rabinowitsch-Mooney relation, with V representing fluid velocity and D denoting pipe diameter. In the context of non-Newtonian laminar flow $8V/D$ is commonly known as the pseudo shear rate, bulk shear rate, or flow characteristic (Slatter, 1995).

Figure 2.9 – Variation of apparent viscosity for a shear-thickening fluid (Created by the author).

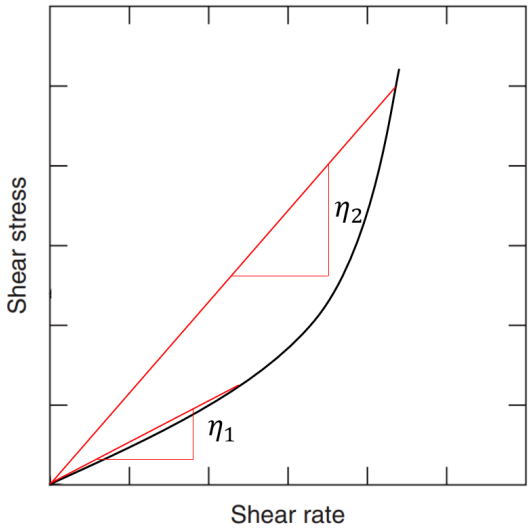

2.3 Laminar single-phase flow of Herschel-Bulkley fluids in circular pipes

This study is focused on the laminar flow of fluids through a circular cross-sectional pipe, particularly applied to fluids exhibiting time-independent or inelastic behavior, also referred to as purely viscous fluids. This model of fluid is characterized by the formation of a solid plug-like core with a radius R_p, flowing through the center of the pipe, when the shear stress is below the yield stress. Furthermore, compared to Newtonian fluids, non-Newtonian fluids usually have high viscosities, making laminar flow more prevalent in engineering practice (Xu; Liao, 2009; Chhabra; Richardson, 2011).

The following equations, proposed by Chhabra e Richardson (2011) and based on the relationship between pressure drop and shear stress, are fully developed with the author's annotations in Appendices A and B.

2.3.1 Shear Stress distribution through force balance analysis

Based on polar coordinates, a cylinder with a radius R and its center on the z-axis is presented in Figure 2.10. Through it, an incompressible fluid with time-independent properties flows along the z-axis with an angular velocity of zero under laminar and fully developed flow. Under these conditions, by performing a force balance, it is possible to relate the pressure drop

gradient $(-\Delta P/L)$ to the shear stress (τ_{rz}) for any position of radius r in relation to the origin of coordinates, as depicted by Equation 2.11.

Figure 2.10 – Flow through a horizontal pipe (Chhabra; Richardson, 2011).

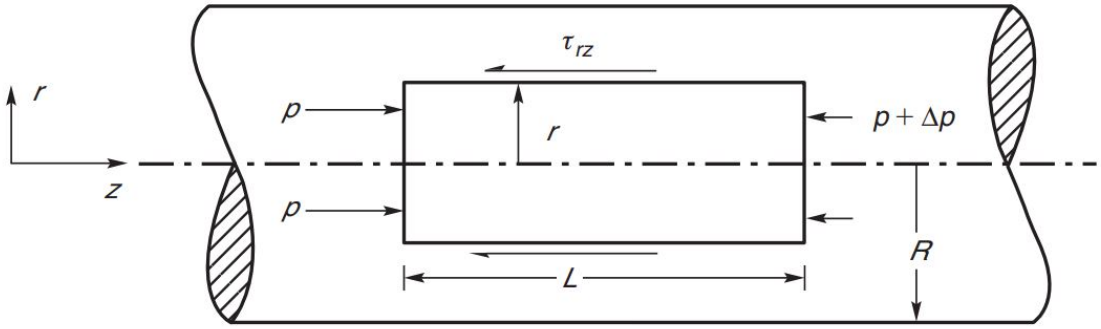

$$\tau_{rz} = \left(-\frac{\Delta P}{L}\right)\frac{r}{2}. \tag{2.11}$$

This relationship developed by Chhabra e Richardson (2011) exhibits a linear distribution profile of the shear stress across the cross section (with variation of r) of the pipe as depicted in Figure 2.11. Thus, the shear stress is zero at the axis of the cylinder ($\tau_{rz} = 0$ for $r = 0$) and reaches its maximum value at $r = R$. Additionally, it is applicable for both laminar and turbulent flow, since it is a simple force balance that does not consider any characteristic property of the flow or the fluid.

2.3.2 Velocity distribution for a Herschel-Bulkley Fluid

A fluid that exhibits a viscoplastic characteristics will only flow if the applied stress, τ_{rz}, exceeds the yield stress value, τ_0^H. In this type of fluid, a solid plug-like core of radius R_p is formed, which flows through the axis of the pipe, where the shear stress is lower than the yield stress. The size of the portion of fluid that behaves like a solid depends on the magnitude of the yield stress and the shear stress on the wall, τ_w, and can be expressed as the relation in Equation 2.12:

$$\frac{\tau_0^H}{\tau_w} = \frac{R_p}{R} = \phi. \tag{2.12}$$

Figure 2.11 illustrates the velocity profile for laminar flow of Bingham plastic or Herschel-Bulkley fluids. The velocity in the plug flow region (V_{zp}) is uniform and is given by Equation 2.13. It is crucial to note that the shear stress is lower than the yield stress within the plug $(r < R_p)$, and these two stresses are equal $(\tau_{rz} = \tau_0^H)$ at the radius of the plug $(r = R_p)$:

$$V_{zp} = \left(\frac{nR}{n+1}\right)\left(\frac{\tau_w}{k}\right)^{1/n}\left[(1-\phi)^{(n+1)/n}\right]. \tag{2.13}$$

Figure 2.11 – Shear stress and velocity distribution for a Herschel-Bulkley or Bingham plastic fluid in a circular cross-section pipe (Chhabra; Richardson, 2011).

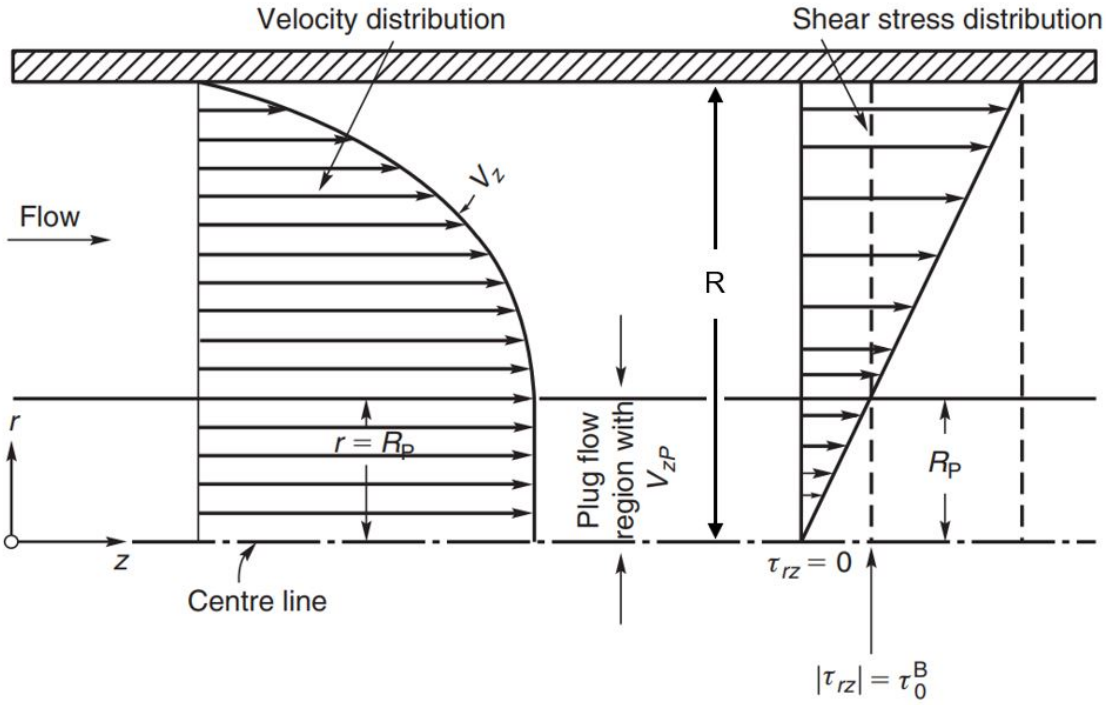

In the annular section, i.e., the space between the radius of the plug and the radius of the pipe $(R_p < r < R)$, the velocity decreases from the constant velocity at the plug to zero at the pipe wall, where τ_{rz} is greater than τ_0^H. Therefore, the velocity distribution (V_z) in the annular space is represented by Equation 2.14:

$$V_z = \left(\frac{nR}{n+1}\right)\left(\frac{\tau_w}{k}\right)^{1/n}\left[(1-\phi)^{(n+1)/n} - \left(\frac{r}{R} - \phi\right)^{(n+1)/n}\right]. \tag{2.14}$$

2.3.3 Volumetric flow rate for a fluid with yield stress

The determination of the volumetric flow rate of a fluid with yield stress, as exposed by Chhabra e Richardson (2011), can be obtained from the equation of the average velocity $\bar{V}$ (Equation 2.15), writing it in terms of flow rate Q (Equation 2.16), and integrating the equation for each flow region. The volumetric flow rate of a fluid with a solid plug-like core is defined as the amount of fluid that passes through a cross section in a given time and is expressed by the Equation 2.17. The detailed derivation of this equation is presented in Appendix B and is represented by Equation B.19:

$$\bar{V} = \frac{Q}{A} \tag{2.15}$$

$$Q = A \times \bar{V} = \int_0^R 2\pi r V_z \mathrm{d}r = \int_0^{R_p} 2\pi r V_{zp} \mathrm{d}r + \int_{R_p}^R 2\pi r V_z \mathrm{d}r \tag{2.16}$$

$$Q = \pi n R^3 \left(\frac{\tau_w}{k}\right)^{1/n} \left[(1-\phi)^{(n+1)/n}\right] \times \left[\frac{2n}{n+1}\left(\frac{1}{2n} - \frac{(1-\phi)^2}{(3n+1)} - \frac{\phi\,(1-\phi)}{2n+1}\right)\right] \quad (2.17)$$

or in terms of average velocity, and considering that $\tau_w = \tau_0^H/\phi$, Equation 2.17 can be rewritten as:

$$\bar{V} = nR \left(\frac{\tau_0^H}{k\phi}\right)^{1/n} \left[(1-\phi)^{(n+1)/n}\right] \times \left[\frac{2n}{n+1}\left(\frac{1}{2n} - \frac{(1-\phi)^2}{(3n+1)} - \frac{\phi\,(1-\phi)}{2n+1}\right)\right] \quad (2.18)$$

3 LITERATURE REVIEW

This chapter details five Reynolds number models, three friction factor correlations, and three equations for calculating pressure drop. These models, equations, and correlations were developed specifically for the internal flow of Herschel-Bulkley fluids in circular cross-section pipes. Additionally, models initially derived for other types of fluids are also presented, as they have been applied to Herschel-Bulkley fluids.

3.1 Reynolds numbers applied to Herschel-Bulkley fluids

3.1.1 Generalized Reynolds number of Metzner and Reed

Metzner e Reed (1955) developed the generalized Reynolds number based on the shear rate model proposed by Rabinowitsch (1929) and Mooney (1931). This model is based on the geometry of the pipe system and not on equations related to fluid regime. The generalized form of the Reynolds number is expressed by Equation 3.1, and it is applicable to Newtonian, Bingham plastic, and Power Law fluids:

$$N_{\text{Re, Metzner}} = \frac{D^n V^{2-n} \rho}{K' 8^{n-1}}, \tag{3.1}$$

where $N_{\text{Re, Metzner}}$ is the generalized Reynolds number, D is the pipe diameter, V is the fluid velocity, ρ is the fluid density, n represents the flow behavior index, also called Power Law index, and K' is the consistency index derivative whose form varies depending on the fluid.

For a Power Law fluid, Metzner e Reed (1955) deduced Equation 3.2 to calculate K':

$$K' = k \left(\frac{3n+1}{4n} \right)^n, \tag{3.2}$$

and for a fluid with yield stress, Metzner (1957) found K' considering the rheological model of a Bingham plastic fluid, obtaining the form of Equation 3.3:

$$K' = \tau_w \left[\frac{k}{\tau_w \left(1 - \frac{4}{3}\phi + \frac{1}{3}\phi^4\right)} \right]^n, \tag{3.3}$$

where τ_w is the wall shear stress and ϕ is the ratio of the yield stress and wall shear stress, established by Equation 2.12.

Finally, in the simplest case, if K' equals μ and n is 1, Equation 3.1 reduces to the Reynolds number for Newtonian fluids.

The Generalized Reynolds number of Metzner and Reed was experimentally validated by the author using carboxymethyl cellulose (CMC), clay, and lime in water.

This work incorporated the generalized Reynolds number combined with K' for Power Law fluids in the analysis because authors like Hanks (1978) and Swamee e Aggarwal (2011) used it to derive their friction factor equations for viscoplastic fluids. It also included the generalized Reynolds number using K' for Bingham fluids because, although K' was not specifically developed for viscoplastic fluid models, it incorporates the variable ϕ.

3.1.2 Reynolds number of Slatter

The approach of Slatter (1995) is based on the fundamental definition of the Reynolds number and it is substituted by the equations proposed by Massey (1980) for the inertial and viscous forces. This dimensionless quantity depicted by Equation 3.4 is also based on the rheological model for yield pseudoplastic flow (Equation 2.9) and the pseudo shear rate, also known as flow characteristic or the bulk shear rate $(8V/D)$, a parameter that was also used by Metzner e Reed (1955) in its formulation:

$$N_{\text{Re, Slatter}} = \frac{8\rho V^2}{\tau_0^H + k(8V/D)^n}. \tag{3.4}$$

It is important to note that Equation 3.4 can be mathematically reduced to the classical Reynolds number by the proportionality constant 8 in the numerator when assuming the parameters for Newtonian fluids ($k = \mu$ and $n = 1$). This reduction was experimentally validated by Haldenwang *et al.* (2012), who used both a Newtonian fluid (water) and ten Herschel-Bulkley fluids (sludge from waste treatment plants).

3.1.3 Reynolds number of Güzel

The Reynolds number of Güzel *et al.* (2009b) was proposed to predict the transition from laminar to turbulent flow in circular-section pipes carrying viscoplastic fluids. To achieve this goal, Güzel *et al.* (2009b) developed their Reynolds number with a different approach, integrating the flow velocity and effective viscosity that vary radially during fluid flow. They considered that the flow velocity at the wall tends to zero, while the effective viscosity at the cylinder axis tends to infinity due to the presence of a portion of the fluid behaving as a solid-like located at the pipe center. These considerations indicate that the Reynolds number tends to zero in both axis and at the pipe wall.

Therefore, Reynolds number of Güzel can be understood as a number that varies radially, reaching its minimum values at the wall and at the cylinder axis, and reaching its maximum value at some point along the cylinder radius. This Reynolds number considers three rheological parameters in its structure, where the yield stress is implicit in the value of ϕ (see Equation 2.12), which represents the relationship between the yield stress and the wall shear stress, and it is calculated by Equation 2.14 using iterative procedures. The Reynolds number of Güzel, presented in Equation 3.5, was validated through experiments focused on identifying the onset of the transitional regime. For this purpose, they used a Newtonian (glycerin), a Power Law (Xanthan gum), and four yield stress fluids (Carbopol®). Additionally, it provided pressure drop predictions with a deviation of up to 16% compared to the measured data in the laminar regime. This equation is given by:

$$N_{\text{Re, Güzel}} = \frac{2\rho V^{2-n} R^n}{k\left(\frac{1}{n}+1\right)^2}\left(1-\phi\right)^{1+n}\left[\frac{\left(1-\phi\right)^2}{\frac{1}{n}+3}+\frac{2\phi\left(1-\phi\right)}{\frac{1}{n}+2}+\frac{\phi^2}{\frac{1}{n}+1}\right]^{n-2}. \tag{3.5}$$

3.1.4 Reynolds number of Madlener

To characterize the flow regime of gelled fuels, Madlener *et al.* (2009) introduced an extended version of the Reynolds number. This dimensionless relationship, illustrated by Equation 3.6, incorporates the wall shear rate expression developed by Rabinowitsch (1929) and Mooney (1931), alongside the extended Herschel-Bulkley equation proposed by Madlener e Ciezki (2005a), Madlener e Ciezki (2005b) that includes the term η_∞ as the constant viscosity in high shear rate range. Due to its versatility, this extended version of the Generalized Reynolds number is also applicable to Newtonian, Power Law, and Bingham plastic fluids.

The Reynolds number of Madlener or HBE-Generalized Reynolds number was tested with Newtonian fluids (paraffin and kerosene) and non-Newtonian gelled fluids (paraffin-thixatrol, paraffin-aerosil, and kerosene-thixatrol-gel) and subsequently compared with the results of the Reynolds number for Newtonian fluids and the Generalized Reynolds number for Power Law fluids of Metzner e Reed (1955). Although Madlener did not provide detailed statistical data about his results, his model showed good graphical agreement with the experimental data for Newtonian fluids and with the results obtained using the Reynolds number for Newtonian fluids.

For non-Newtonian gelled fluids, Madlener's model presented graphically better results than the Newtonian fluid model and Metzner and Reed model for Reynolds number

values below 200. However, for Reynolds numbers greater than 200, the model tended to overestimate the friction factors compared to the experimental values, an observation for which Madlener acknowledged he did not have an explanation.

The Reynolds number according to Madlener is expressed as follows:

$$N_{\text{Re, Madlener}} = \frac{\rho V^{2-n} D^n}{\frac{\tau_0^H}{8}\left(\frac{D}{V}\right)^n + k\left(\frac{3m+1}{4m}\right)^n + \eta_\infty\left(\frac{3m+1}{4m}\right)\left(\frac{D}{V}\right)^{n-1}}, \tag{3.6}$$

$$m = \frac{nk\left(\frac{8V}{D}\right)^n + \eta_\infty\left(\frac{8V}{D}\right)}{\tau_0^H + k\left(\frac{8V}{D}\right)^n + \eta_\infty\left(\frac{8V}{D}\right)}. \tag{3.7}$$

3.2 Equations and correlations for internal flow of Herschel-Bulkley fluids in laminar regime

Friction is vital in fluid dynamics since it denotes the resistance between the fluid and the surfaces in contact, opposing sliding and impacting the pressure drop. It is determined by calculating the Fanning friction factor (f) or Darcy friction factor (f_D), which is four times the Fanning friction factor $(4f = f_D)$.

In laminar regimes and Newtonian fluids, the Fanning friction factor is a function of the Reynolds number and is governed by Equations 3.8:

$$f = \frac{16}{N_{\text{Re}}} = \frac{16\mu}{VD\rho}, \tag{3.8}$$

and, as detailed by Bourgoyne *et al.* (1986), for any fluid the Fanning friction factor is related to pressure drop (ΔP) through the Fanning equation as indicated by Equation 3.9:

$$f = \frac{\Delta P D}{2L\rho V^2}. \tag{3.9}$$

For Herschel-Bulkley fluids, multiple equations for pressure drop and friction factor have been proposed over the last 70 years, with no consensus on which model accurately captures the friction and the pressure drop phenomenon, as Abou-Kassem *et al.* (2023) also recently observed. The following sections will present and discuss various models from the literature used in this study.

3.2.1 Friction-factor correlation of Hanks

Hanks (1978) formulated the first theoretical correlation (Equation 3.10) for the friction factor of Herschel-Bulkley fluids in a laminar flow regime, using the Generalized Reynolds

number for Power Law fluids of Metzner and Reed (Equations 3.1 and 3.2) and the Fanning friction factor as basis:

$$f = \frac{16}{\psi N_{\text{Re, Metzner (PL)}}} \tag{3.10}$$

where:

$$\psi = (1+3n)^n (1-\phi)^{1+n} \left\{ \frac{(1-\phi)^2}{3n+1} + \frac{2\phi(1-\phi)}{2n+1} + \frac{\phi^2}{n+1} \right\}^n .$$

Although Hanks did not experimentally validate his formulation, this correlation has proven to have good approximations for smooth pipes, as indicated by Heywood e Cheng (1984). They conducted one of the earliest comparative studies about available equations applied to Herschel-Bulkley fluids to predict the friction factor in both laminar and turbulent regimes, and the Hanks (1978) correlation was presented as the only available model for the laminar regime up to 1984. Heywood e Cheng (1984) also emphasized in their study the complexity associated with determining rheological properties of non-Newtonian fluids, highlighting its high sensitivity to the exact composition and homogeneity of the fluid. Additionally, they suggested employing various friction factor prediction methods for Herschel-Bulkley fluids to establish a range of maximum and minimum values of friction. Subsequently, through engineering judgment, the most suitable value or range of values could be selected to predict pressure drop.

Subsequently, Garcia e Steffe (1986) added that Hanks' analysis represented the most comprehensive study related to Herschel-Bulkley fluids and then validated the correlation experimentally with Power Law, Bingham plastic, and Newtonian fluids. Additionally, Garcia e Steffe (1986) concluded that predicting the friction factor in fluids that display yield stress using models based on fluids without yield stress carries a considerable risk of error. These projections may be overestimated or underestimated, depending on the values of the parameters n, N_{Re}, and He.

3.2.2 Friction-factor correlation of Güzel, Frigaard and Martinez

Based on experiments with Carbopol® 940, Güzel *et al.* (2009b) proposed a friction factor correlation for fluids with yield stress flowing in laminar regime. This proposal (Equation 3.11) considers the ratio of the solid-like plug velocity at the cylinder axis (u_c) to the mean velocity of the fluid (U_b). The Güzel *et al.* (2009b) correlation expressed in Fanning friction factor terms, is given by:

$$f = \frac{1}{4} \times \frac{16}{N_{\text{Re,Güzel}}} \left(\frac{u_c}{U_b} \right)^2 , \tag{3.11}$$

where:

$$\frac{u_c}{U_b} = \frac{\left(\frac{1}{n}+2\right)\left(\frac{1}{n}+3\right)}{2\phi^2 + 2\left(\frac{1}{n}+1\right)\phi + \left(\frac{1}{n}+2\right)\left(\frac{1}{n}+1\right)}.$$

3.2.3 Friction-factor correlation of Swamee and Aggarwal

Subsequently, Swamee e Aggarwal (2011) proposed the Equation 3.12, a theoretical expression for the friction factor based on the Generalized Reynolds number for Power Law fluids of Metzner e Reed (1955) (Equations 3.1 and 3.2), specially developed for Herschel-Bulkley fluids in the laminar regime. This correlation was not experimentally validated by the author, however, it was presented as an explicit version of the theoretical Hanks (1978) equation, to avoid the necessity of iterative procedures in its resolution and to optimize computational time in simulations. The correlation is defined as:

$$f = \frac{16}{N_{\text{Re, Metzner(PL)}}} + \frac{16}{N_{\text{Re, Metzner(PL)}}} \times \left\{ \frac{He}{\left[36 + \left(\frac{3}{2n}\right)^{2.46}\right]^{0.5} N_{\text{Re, Metzner(PL)}}} \right\}^{0.958n/(2-n)}, \quad (3.12)$$

where the Hedstrom number is given by:

$$He = \frac{D^2\rho}{k}\left(\frac{\tau_0^H}{k}\right)^{(2-n)/n}.$$

3.2.4 Pressure drop equation of Metzner and Reed

Applying the principles detailed in Section 3.1.1 to develop the Generalized Reynolds number, and relating it with ΔP from Equation 3.9, Metzner e Reed (1955) proposed Equation 3.13 to calculate the pressure drop of Newtonian, Bingham plastic, and Power Law fluids in laminar regime:

$$\Delta P = \frac{32K'8^{n-1}V^n}{D^{n+1}}. \quad (3.13)$$

3.2.5 Pressure drop equation of Chilton and Stainsby

Chilton e Stainsby (1998) developed a novel approach to calculate pressure drop in both Newtonian and non-Newtonian fluids, without considering the friction factor and addressing flow conditions in the laminar and turbulent regimes. They adopted the Herschel-Bulkley model to describe fluid rheology, considering it as the most comprehensive approach, since it can be reduced to other rheological relationships: the Bingham plastic (if $\tau_0 > 1$ and $n = 1$), Power Law (if $\tau_0 = 0$ and $n < 1$), and Newtonian (if $\tau_0 = 0$ and $n = 1$) models, as also demonstrated by Slatter (1995).

Chilton e Stainsby (1998) concluded that their approach (Equation 3.14) provided consistent solutions of pressure drop within a 15% error margin for both laminar and turbulent flows for non-Newtonian fluids. This equation was validated by comparison with experimental data from two other research works, which used viscoplastic fluids such as kaolin slurry and sewage sludge. Their equation is given by,

$$\frac{\Delta P}{L} = \frac{4k}{D}\left(\frac{8V}{D}\right)^n \left(\frac{3n+1}{4n}\right)^n \left(\frac{1}{1-\phi}\right)\left(\frac{1}{1-a\phi-b\phi^2-c\phi^3}\right)^n, \tag{3.14}$$

where:

$$a = \frac{1}{2n+1}; b = \frac{2n}{(n+1)(2n+1)}; c = \frac{2n^2}{(n+1)(2n+1)}.$$

3.2.6 Pressure drop equation of Chhabra and Richardson

Assuming that the flow of an incompressible fluid through a circular pipe is induced by a pressure difference, Chhabra e Richardson (2011) proposed a relationship between the pressure gradient and the shear stress, obtained through a force balance. This relationship, as defined by Equation 3.15, is valid for both laminar and turbulent regimes and for various types of fluids, as the development of the equation does not consider mean flow velocity, V, or rheological parameters such as n and k, as demonstrated in Appendix A

$$\tau_w = \left(-\frac{\Delta P}{L}\right)\frac{D}{4}. \tag{3.15}$$

For the specific case of the Herschel-Bulkley model, the value of the force that the fluid exerts tangentially on the surface of the pipe (i.e., the wall shear stress) is influenced by the yield stress, τ_0^H, and the ratio between the solid plug-like core radius and the pipe radius, $\phi = R_p/R$, as stated by Equation 3.16:

$$\tau_w = \frac{\tau_0^H}{\phi} = \frac{\tau_0^H R}{R_p}. \tag{3.16}$$

Therefore, substituting Equation 3.16 into Equation 3.15 and solving for ΔP, it is obtained Equation 3.17, which provides similar pressure drop predictions to those obtained by the Chilton e Stainsby (1998) equation. However, Equation 3.17 was derived in a simpler manner than Equation 3.14:

$$\frac{\Delta P}{L} = \frac{4\tau_0^H}{\phi D} \tag{3.17}$$

The pressure drop predictive capability of all these models, equations, and correlations will be experimentally evaluated in Chapter 5. If the analytical results do not closely match the experimental data (with a difference of less than $\pm 10\%$), the analysis proposed in Chapter 4 will be applied to improve their performance.

4 MATERIALS AND METHODS

This chapter presents the methodology and procedures used during the experimental tests to investigate the pressure drop during the single-phase flow of viscoplastic fluids inside pipeline. The subsequent section details the concentration of the fluid components, the preparation of working fluid, the rheology measurements, the experimental apparatus, the procedure for the experiments, and the instrumentation used for data collection.

4.1 Working fluid

The fluid model used to replicate the Herschel-Bulkley behavior during experiments was composed by tap water, Carbopol® 940, and a solution of Triethanolamine.

The water-soluble synthetic polymer Carbopol was developed and trademarked by Lubrizol Corporation in Wickliffe, OH, USA. It is highly appreciated in the research community due to its behavior, which resembles an idealized yield stress fluid. This fluid characteristic makes it particularly useful for predicting yield stress and viscosity magnitudes. Additionally, its transparency facilitates flow visualization studies. Beyond its research applications, Carbopol rheology modifier is widely used in various industries as a thickening agent, suspension stabilizer and emulsifier (Curran *et al.*, 2002; Varges *et al.*, 2019).

Carbopol is a crosslinked high molecular weight polyacrylic acid polymers and can be classified as homopolymers, copolymers and interpolymers (Lubrizol, 2023). Carbopol 940 is presented in the form of a dry white powder with an average particle size of 0.2 micrometers (Lubrizol, 2007b; Lubrizol, 2022). These particles, composed of coiled acidic molecules, undergo a process of hydration and partial uncoiling upon contact with water. Carbopol solution has a pH range of 2.5 to 3 (Lubrizol, 2009).

A common procedure to increase the viscosity of the Carbopol solution involves transforming it into a salt (Lubrizol, 2009). This process is carried out through neutralization of pH with a common base, such as sodium hydroxide (NaOH), aminomethyl propanol, or Triethanolamine (TEA) (Iceri *et al.*, 2023). In this work, the Triethanolamine, which belongs to the ethanolamine family, was employed. Pure ethanolamines are colorless liquids that dissolve readily in most polar solvents like water and alcohol, with Triethanolamine being the most polar among them due to its three hydroxyl radical groups in its structure (Knaak *et al.*, 1997).

The concentration of Triethanolamine and Carbopol influence the molecular structure of a fluid in different ways. An increase in the concentration of Triethanolamine while keeping the concentration of Carbopol constant, results in an increase in bonds between the carbomer molecules. On the other hand, increasing Carbopol for the same Triethanolamine concentration increases the number of carbomer molecules per unit of mass, which, in both cases, leads to an increase in the yield stress (Iceri *et al.*, 2022; Iceri *et al.*, 2023).

4.1.1 Concentrations

The best concentrations of Carbopol and Triethanolamine to prevent the formation of fungi and achieve a stable and homogeneous solution with gel-like behavior were determined in the laboratory-scale study (Iceri *et al.*, 2023). The optimal procedure for preparing the solution was also defined in small-scale tests. Subsequently, this small sample was scaled up to increase the solution volume for testing in a closed flow loop. The detailed concentration of sample is provided in Table 4.1.

Table 4.1 – Summary of Carbopol and Triethanolamine concentrations.

Components	**Sample 1**
Tap water	800 L
Carbopol	0.15 % (1202 gr)
Triethanolamine	750 ppm (600 gr)

4.1.2 Preparation of the polymer solution

The procedure used to prepare the working fluid was based on the method proposed by Iceri *et al.* (2023). The steps are illustrated in Figure 4.1:

Figure 4.1 – Flowchart of the working fluid preparation procedure.

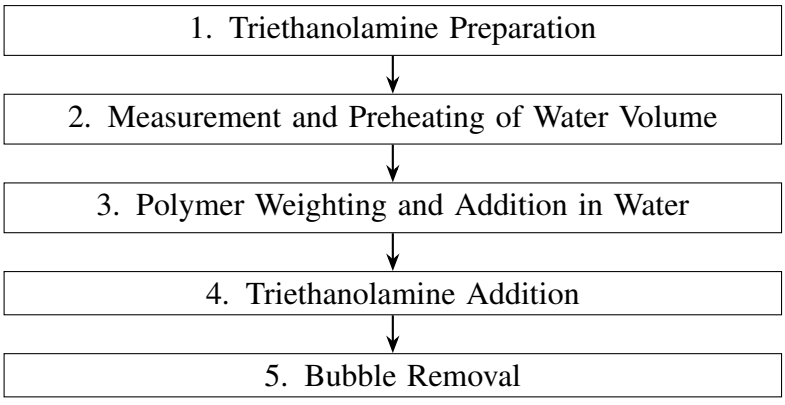

Triethanolamine preparation:

1. It was employed a drying and sterilization oven, subjecting its interior to a 2-hour heating process until a stable temperature of 50°C is attained.
2. The solid Triethanolamine was positioned within the oven for 24 hours until it liquefies.
3. Subsequently, the dilution process was performed by blending the liquid Triethanolamine with ionized water to achieve a mass concentration of 85% Triethanolamine and 15% water.

Measurement and preheating of water volume:

4. To prepare the experimental fluid, according to the dimension of the flow loop, it was determined that a minimum volume of 800 liters of tap water was required.
5. That specified tap water volume was preheated to 45°C within a reactor to improve conditions for polymer dispersion.

Polymer weighting and addition in water:

6. The polymer quantity indicated in Table 4.1 was weighted using an analytical balance to achieve the targeted concentration.
7. Then, the Carbopol was added in 100-gram increments into the water in the reactor while stirring at 15 rpm to prevent lump formation.
8. For each batch of 400 grams of Carbopol added to the water volume, stirring was increased to 40 rpm and held for 3 minutes to enhance the dissolution of the component.
9. Upon the complete incorporation of the total mass of Carbopol, a consistent stirring rate of 20 rpm for 12 hours was applied, to guarantee complete homogenization of the solution.
10. In this step is essential to highlight that, despite the hydrophilic nature of Carbopol and the quick wetting of their particles when individually dispersed, improper incorporation into the water can lead to the formation of powder aggregates. In this scenario, solvation occurs on the surface of the powder aggregate, which can form a heterogeneous solution. This process yields a dispersion with a granular texture, low viscosity and insoluble particles (Lubrizol, 2007a). Hence, varying the stirring speed during preparation is necessary to ensure proper homogenization of the solution.

Triethanolamine addition:

11. The solution of Triethanolamine was carefully added in 50 ml increments, followed by agitation of the fluid at 20 rpm for 3 minutes after each increment.

12. Upon total inclusion of the Triethanolamine, a stirring speed of 40 rpm was maintained for 24 hours to guarantee complete solution uniformity and chain stability.

Bubble removal:

13. Finally, a vacuum process of 240 mBar within the reactor was applied for 1 hour.

14. After that, the reactor was kept in vacuum with a stirring of 20 rpm for 12 hours. The aim was to eliminate the microbubbles that may have been trapped in the solution during the stirring process in the preparation phase, due to the viscoplastic nature of the fluid. This procedure is essential to ensure a single-phase flow, as the microbubbles cannot escape solely due to buoyancy effects because of the fluid's yield stress. Once the process is completed, a fluid sample was collected to perform rheological characterization to verify if the desired parameters were achieved.

4.1.3 Rheological measurements

Multiple samples were collected from the reactor after the preparation procedure and from the flow line before changing the flow rate during the experimental test. The rheological parameters were evaluated at 25°C using a Thermo Scientific Haake Mars III rheometer, employing serrated parallel plates (Figure 4.2) to prevent slippage when measuring the flow curve tests.

The parallel plates have a diameter of 35 mm, and a gap of 1 mm was used in the rheological tests.

The rheological parameters were determined using the flow curve method, working with a shear stress range of $0.1\,\text{Pa} < \tau < 100\,\text{Pa}$. Data were measured after 15 seconds to achieve steady-state at each shear stress point, and 100 points were obtained during the test.

Figure 4.2 – Serrated parallel plates of Thermo Scientific Haake Mars III rheometer (Created by the author).

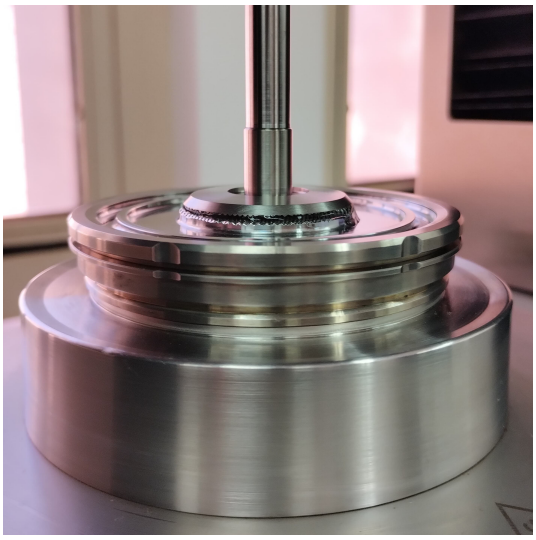

4.2 Experimental apparatus

The experiments were conducted at the experimental apparatus of the Petroleum Experimental Laboratory (LabPetro) at the Center for Energy and Petroleum Studies (CEPETRO) at the Universidade Estadual de Campinas (UNICAMP).

A schematic diagram of the flow loop facility used in the experiments is illustrated in Figure 4.3, while Figures 4.4 and 4.5 provide photographs of the flow loop circuit, and Figure 4.6 shows the visualization section. Detailed technical specifications of the flow loop components and measurement instruments can be found in Sections 4.2.1 and 4.2.2, respectively.

In the flow loop circuit configuration, the progressive cavity pump 1 carries the Carbopol solution from the reactor to Tank 1. Progressive cavity pump 2, situated at the bottom of Tank 1, provides the necessary energy to displace the fluid through the flow loop. Right away, the flow passes through the shell and tube heat exchanger to adjust the fluid temperature according to the parameters set for the water temperature in the control system (chiller and thermoregulator) to maintain the fluid at the test section at 25 °C. Subsequently, a Coriolis-type flow meter sensor installed in the flow line measures the mass flow rate $(\dot{m}_l)$ data. After a flow development length of 20 m, the test section is positioned and over it, the pressure drop (ΔP) sensor is allocated with a 2.4 m distance. Additionally, absolute pressure (P) and temperature (T) data at the inlet (1) and outlet (2) of the test section have been acquired. Upon completing its passage through the test section, the fluid returns to a set of three valves that can direct the flow to different tanks: a) to reservoir Tank 1 to maintain a closed flow loop, b) to the

reactor in case to eliminate microbubbles trapped in the fluid and, alternatively, c) the fluid can be directed to Tank 2 to discard the volume if fluid degradation is detected.

Figure 4.3 – Schematic diagram of the flow loop facility used in the experiments (Created by the author).

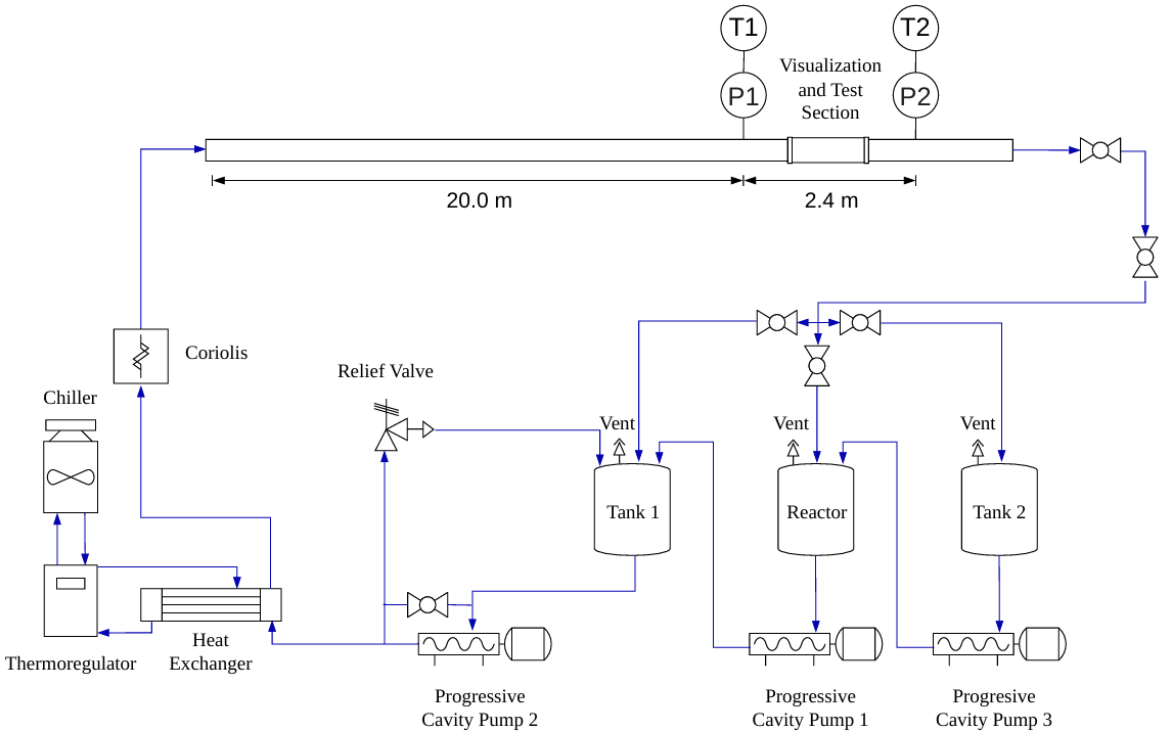

Figure 4.4 – Photograph of the experimental apparatus with emphasis on equipments in the containment basin (Created by the author).

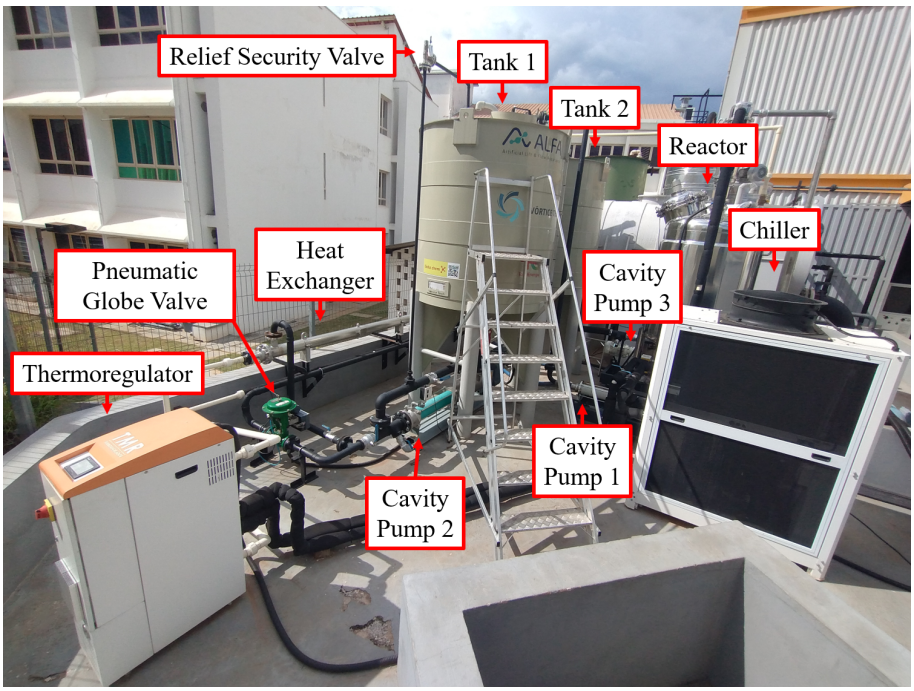

Figure 4.5 – Photograph of the experimental apparatus with emphasis on flow line (Created by the author).

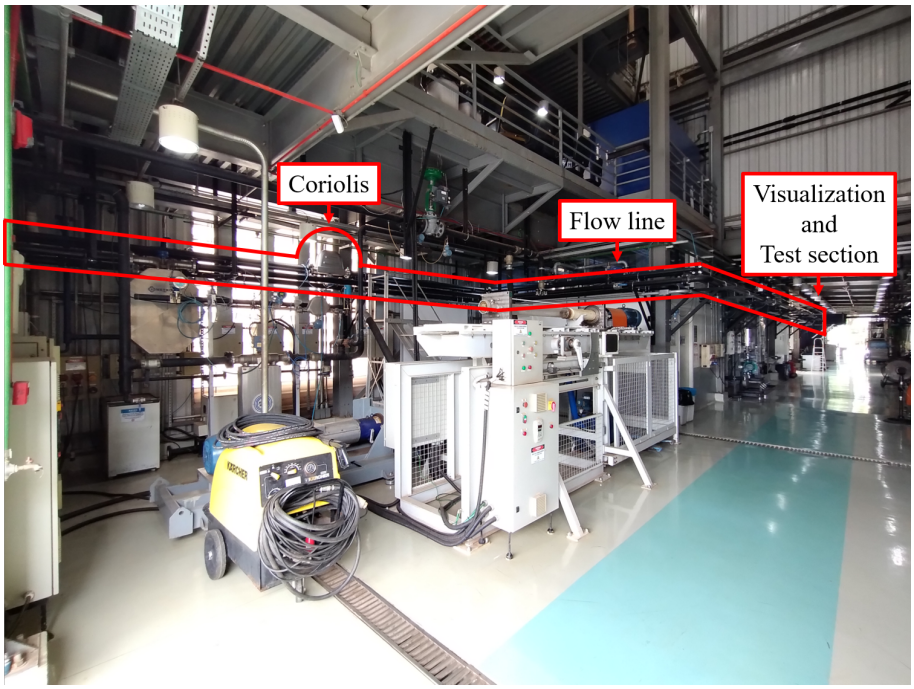

In the visualization section of the test section, a high-speed camera was positioned to assess the presence of bubbles in the fluid. If bubbles are detected, the procedure for eliminating bubbles from the fluid through heating, vacuum, and agitation was initiated.

Figure 4.6 – Photograph of visualization section placed in the test section (Created by the author).

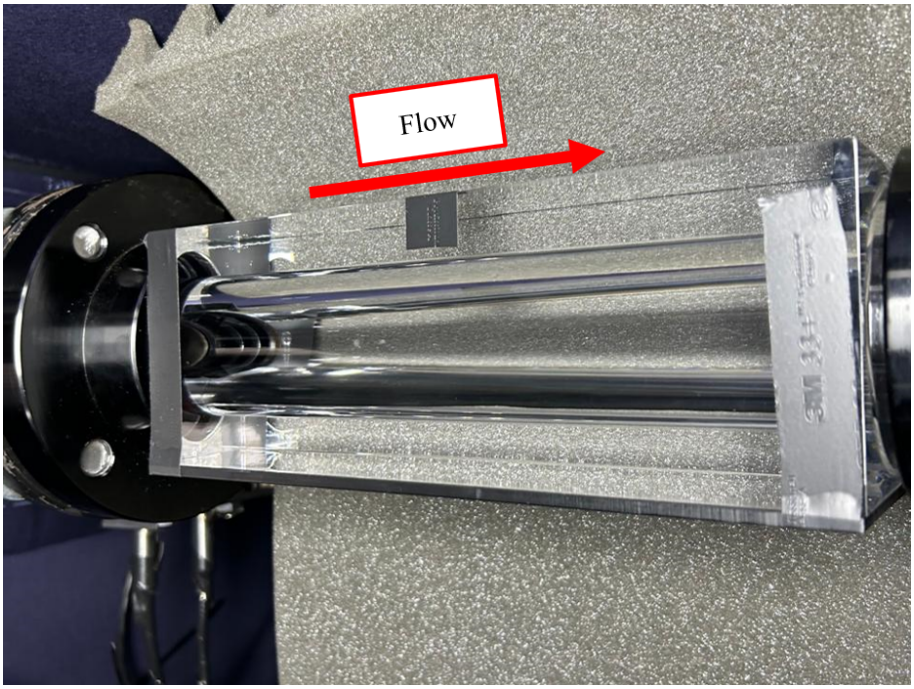

4.2.1 Flow loop components

A detailed description of experimental equipments can be found in Table 4.2:

Table 4.2 – Description of the experimental apparatus equipment.

Component	**Manufacturer/Model**	**Quantity**	**Characteristics**
Steel Pipe	-	-	Standard galvanized, internal diameter = 0.05386 m, roughness = 0.00006 m
Reactor	Metalquim	1	Maximum capacity of 1000 L
Tank	Vórtice Tech	2	Polypropylene material, maximum capacity of 3000 L
Vacuum Pump	Busch Mink MM 1252 AV	1	vaccum pressure range 210-240 mBar
Progressive Cavity Pump 1 & 3	Netzsch NM053BY02S14V	2	Displacement pump, maximum flow rate 5.2 (m^3/h), pressure 10 bar, power 4.2 cv.
Progressive Cavity Pump 2	Netzsch NM063BY02S14V	1	Displacement pump, flow rate range 0.35 - 9 (m^3/h), pressure 10 bar, power 7.2 cv.
Pump motor 1 & 3	SEW Eurodrive FF57 DRN112MP4	2	Power supply 220 - 440 V, f = 60 Hz, rotation speed 215 - 1764 rpm.
Pump motor 2	SEW Eurodrive FF77 DRN132MP4	1	Power supply 220 - 440 V, f = 60 Hz, rotation speed 190 - 1771 rpm.
Frequency inverter Pump	WEG CFW500	1	Variable Speed Drive, power range 0.25 - 175 cv, output current 1.0 - 211 A, 200 to 240 V.
Relief Security Valve	-	1	Opening pressure 4 bar
Pneumatic Globe Valve	Fisher Design GX	1	
Heat Exchanger	Fyterm	1	Shell tube, heat exchange area 1.4 m^2
Chiller	Mecalor MSA-30-RI-380	1	Power supply 380V, f=60Hz, Work Temperature 5 - 25°C
Thermoregulator	Mecalor TMR-M-18-380/C	1	Power supply 380V, f=60Hz, Work Temperature 10 - 90°C

4.2.2 Measurement Instruments

As detailed in Table 4.3, four variables are measured during the experiments: liquid mass flow rate, temperature, absolute and differential pressure.

Table 4.3 – Description of the measurement Instruments.

Variable	Equipment	Manufacturer / Model	Uncertainties	Characteristics
$\dot{m}_l$	Liquid Mass Flow Meter	Emerson MicroMotion R200S4	0.1% of absolute value	Coriolis Type, Temperature -100 to 150 °C, Out 4-20mA, 0-87100 kg/h
ΔP	Differential Pressure Sensor	Emerson Rosemount 3051CD	0.1% of span (equivalent to 60 Pa)	Differential pressure gauge, Out 4-20 mA, 0-62000 Pa
T	Temperature Sensor	Sensym TR106	± 0.1 ºC at 25 ºC	Thermoresistive sensor, PT100 type, Resistance tolerance of 1/10 DIN, 0-100 ºC

A Coriolis-type sensor installed in the flow line measures the mass flow rate $(\dot{m}_l)$ data. Equation 4.1 allows the calculation of the average flow velocity $(\bar{V})$ for a single-phase flow based on these mass flow data. The Carbopol solution density was assumed to be equal to that of water (998 kg/m^3) since the quantities of the components only represent $0.22\,\%$ of the total mass.

$$V = \frac{\dot{m}_l}{3600\rho A}. \tag{4.1}$$

The cross-sectional area (A) of the pipe was determined by the internal diameter of the pipe using a Vernier caliper. The internal diameter (D) is equal to $0.05386 \pm 0.19 \times 10^{-3}$ m. Due to the uncertainty associated with the diameter, the velocity has a propagated uncertainty of $\pm$ 0.71% relative to the measured value.

During the experiment, the data collected by the sensors are displayed in real time through the graphical user interface (Figure 4.7) of a monitoring program developed in LabVIEW® 2016. The program is integrated with an instrumentation panel composed of two input modules and two output modules connected to a National Instruments NI cDAQ-9189 chassis.

The Coriolis and pressure sensors information are sent to the current input module NI-9203, while the data from the PT100 temperature sensors is received through the input module NI-9217. Furthermore, the program enables remote control of the equipment through the output modules. The rotation of the pump motor is linked to both current actuator control module NI-9266 and a frequency inverter WEG CFW500. Further details of each module are available in Table 4.4.

Figure 4.7 – LabVIEW® graphical user interface.

Table 4.4 – Description of the instrumentation panel components.

Device	Manufacturer / Model	Characteristics
Chassis for signal acquisition modules	National Instruments NI cDAQ-9189	8-Slot, Ethernet chassis, Data transfer between I/O modules
Current Input module	National Instruments NI-9203	8-Channel, Receives signal from Coriolis ($\dot{m}_l$) and pressure sensors (ΔP), Input range 4-20 mA
Temperature Input module	National Instruments NI-9217	4-Channel, Resistance Temperature Detector (RTD), Signal range 100 Ohm
Voltage Output module	National Instruments NI-9263	4-Channel, Output voltage signal controls the frequency inverter of the pump, Voltage Output range $\pm$ 10 V
Current Output module	National Instruments NI-9266	4-Channel, Output current signal for control of the pneumatic globe valve, Current Output range 4-20 mA.

4.3 Methods

To analyze the results, the following 12-step workflow depicted in Figure 4.8 has been developed to examine the data collection, evaluate the Reynolds number models, friction factor correlations and determine if there is any suitable combination to more accurately predict pressure drop.

Figure 4.8 – Data analysis workflow (Created by the author).

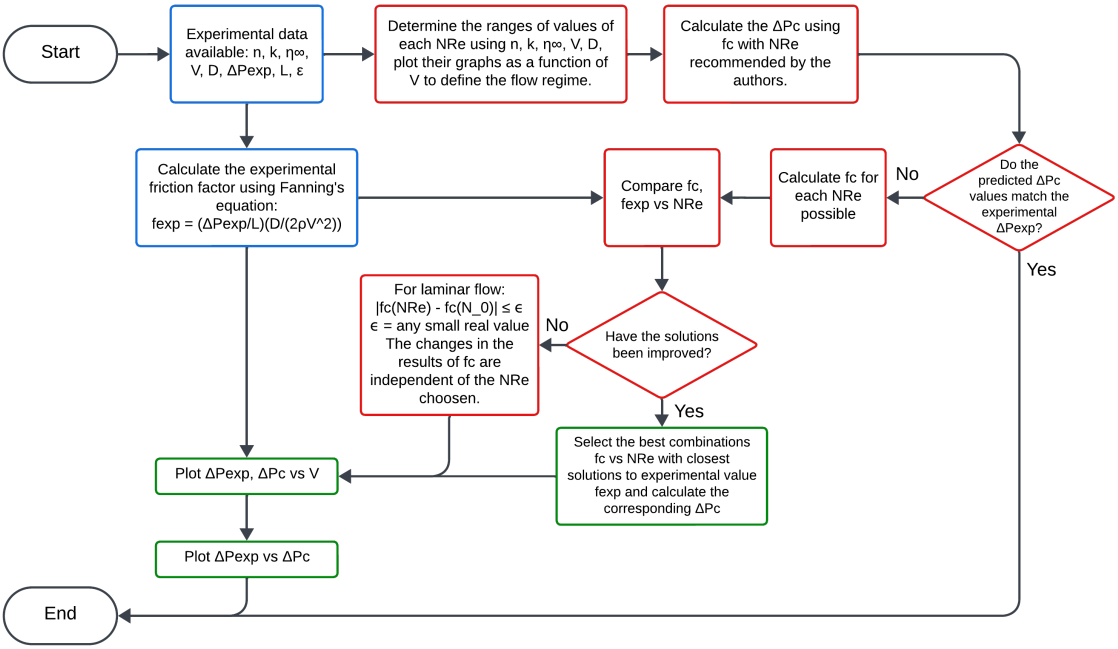

4.3.1 Data analysis workflow

Blue steps

1. During the experimental tests, pressure drop (ΔP_{exp}) and flow mean velocity $(\bar{V})$ are measured. Subsequently, following the procedure from Section 4.1.3, the flow curve of the working fluid is measured in the laboratory. Through curve fitting, the values of the rheological parameters Power Law index (n), consistency index (k), and constant viscosity for a high range of shear rates (η_∞) were obtained.

2. Calculate the experimental friction factor (f_{exp}) using the data from step 1 and Fanning's equation (Equation 3.9) to perform a comparative analysis with the analytical friction factors to be calculated in step 6.

Red steps

3. Plot trend curves for each Reynolds number (N_{Re}) model as a function of mean flow velocity $(\bar{V})$ using the data from step 1 and Equations 3.1, 3.4, 3.5 and 3.6. Then, select the friction factor correlations according to the flow regime identified by each Reynolds number.

4. Calculate the predicted pressure drop (ΔP_c) using Equation 3.9 and taking into account the different correlations for the friction factor (f_c), together with their respective recommended Reynolds number models.

5. Do the predicted pressure drop (ΔP_c) values from step 4 match the experimental measured pressure drop values (ΔP_{exp})? If the values are close or coincide, the analysis is concluded; otherwise, proceed to the next step.

6. In order to verify if it is possible to improve the results, it is proposed to calculate new values for the friction factor (f_c) using all possible combinations between friction factor correlations and Reynolds number models that were not recommended by the own studies. This will be done by combinatorial analysis.

7. Plot in a single figure the experimental friction factor (f_{exp}) calculated in step 2 and the new predicted friction factor (f_c) values calculated in step 6, to observe whether any new combination of friction factor and Reynolds number is closer to the experimental values than the friction factor values obtained in step 4.

8. Do the new results from step 6 and 7 show an improvement in the friction factor prediction?

9. If the answer is negative, it can be interpreted that, for the laminar regime, the value of the predicted friction factor will not vary significantly regardless of the chosen Reynolds number model. Therefore, the difference between the friction factors calculated with two different Reynolds number models will be insignificant.

Green steps

10. If the answer to the question in step 8 is yes and there is an improvement in the results, the new predicted pressure drop (ΔP_c) will be calculated using the best combination of friction factor correlation and Reynolds number model.

11. Plot in a single figure the measured pressure drop (ΔP_{exp}) and the new predicted pressure drop (ΔP_c), calculated in step 10, as a function of mean flow velocity $(\bar{V})$.

12. Finally, to obtain the statistical analysis, the measured pressure drop (ΔP_{exp}) is plotted versus the new predicted pressure drop (ΔP_c) from step 10.

4.4 Performance metrics

The accuracy of the calculated data relative to the experimental data was assessed using the Mean Absolute Error (MAE). This widely recognized metric offers a simple and efficient measure of the average magnitude of error. As the MAE decreases, it reflects a greater accuracy of the employed method (Ostertagova; Ostertag, 2012). The formula to calculate MAE is expressed as:

$$MAE = \frac{1}{m}\sum_{i=1}^{m}|y_i - \hat{y}_i| \tag{4.2}$$

where y_i is the measured or true data, $\hat{y}_i$ is the predicted data and m is the number of fitted points.

To represent the average absolute percentage deviation of the forecasts in relation to the observed values, the Mean Absolute Percentage Error (MAPE) was calculated, which is based on the relative error. A low MAPE indicates that the predicted values are close to the reference values, demonstrating greater accuracy in the predictions made (Ostertagova; Ostertag, 2012). The formula for calculating the MAPE is expressed as:

$$MAPE = \frac{1}{m}\sum_{i=1}^{m}\left|\frac{y_i - \hat{y}_i}{y_i}\right| \times 100\%. \tag{4.3}$$

5 RESULTS AND DISCUSSIONS

The results will be presented in this chapter and are structured in the following subsections: (a) experimental data measured in single-phase flow and laminar regime within a circular cross-sectional flow loop using a Herschel-Bulkley fluid. (b) The combinatorial analysis, described in Section 4.3.1, developed using the different friction factor correlations and Reynolds number models. This analysis evaluated how the various friction factor-Reynolds number combinations behave about the experimental data to identify the best options for predicting the pressure drop. Finally, (c) contrasting the best friction factor-Reynolds number combinations from prior analysis with data from literature provided additional validation of the accuracy and applicability of the chosen models.

The analysis of the results are discussed following the flowchart presented in Figure 4.8 and described in Section 4.3.

5.1 Experimental data

The validation of the differential pressure sensor was conducted with single-phase tests using water before starting the experimental test with the non-Newtonian fluid. Further details are provided in Appendix C.

In the experimental test with the Herschel-Bulkley fluid, various fluid samples were collected to analyze mechanical degradation. The first sample was taken at the beginning from the reactor to be used as a reference. Subsequently, a sample was collected for each rotation, corresponding to each experimental point.

The rheological data of the fluid samples were determined using a rheometer via the flow curve test (Figure 5.1). This methodology provides a shear stress (τ_{yx}) versus shear rate $(\dot{\gamma}_{yx})$ curve. By applying curve fitting, the yield stress (τ_0^H) and consistency index (k) were calculated, with the Power Law index (n) being 0.5, as indicated in the study by Caggioni *et al.* (2020).

The measured rheological parameters of the collected samples indicated minimal variation in the fluid's properties throughout the experimental test. Table 5.1 presents the mean value and standard deviation for the rheological parameters:

Table 5.1 – Rheological parameters of the working fluid.

τ_0^H **(Pa)**	n **(-)**	k **(Pa.s^n)**	η_∞ **(Pa.s)**	ρ **(kg/m^3)**
7.67 ± 1.6	0.5	1.83 ± 0.21	0.001	998

Figure 5.1 – Flow curve for 0.15 wt% Carbopol and 800 ppm of Triethanolamine.

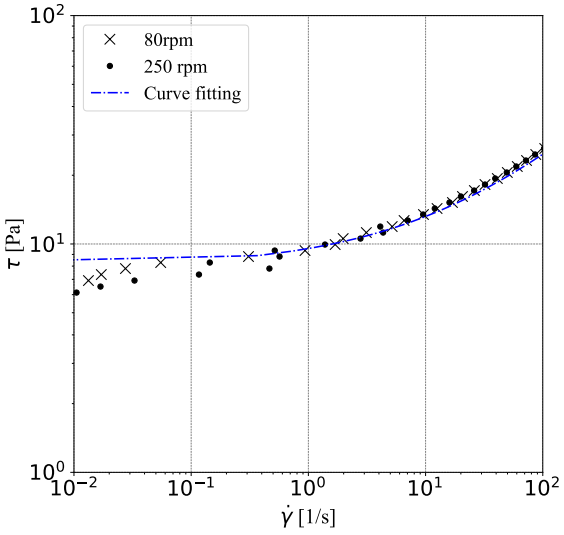

As the experiment progressed, the rheological properties were monitored for each pump rotation, and when the rheological parameters of the fluid dropped below the initial reference sample minus its standard deviation, the test was concluded. Due to the rheological degradation of the working fluid, a reduced number of experimental points were collected during the test to maintain the quality of results.

The single-phase flow test was conducted by controlling the pump rotation, resulting in measurements of mass flow rate ($\dot{m}_l$), pressure drop (ΔP_{exp}), and fluid temperature (T_{in} and T_{out}) measured at the inlet and outlet of the test section. Furthermore, the temperature was kept stabilized at $\sim 25\,^{\circ}$C in the course of testing to minimize its influence on the rheological properties, ensuring they remain stable within the standard deviation and unaffected.

The collected data is detailed in Table 5.2. Additionally, the mean flow velocity ($\bar{V}$), calculated from the mass flow rate using Equation 4.1 is also provided. The relationship between pressure drop and mean flow velocity from Table 5.2 is plotted in Figure 5.2. As expected, the measured pressure drop increased proportionally with the square of the mean flow velocity ($\Delta P \propto \bar{V}^2$), as expressed by Equation 3.9. And, in the special case of a Herschel-Bulkley fluid, it was also anticipated that the slope of the pressure drop curve might be different and would

decrease as the velocity increased, due to the shear-thinning nature of this type of fluid.

Thus, considering the theoretical foundations, the most remarkable aspect of Figure 5.2 is that the measured data show an apparent linear trend (blue dotted line) between the pressure drop and the velocity. The apparent linear trend could be justified because the measured experimental data fell within a low-velocity range, which does not clearly allow to distinguish this phenomenon of decreasing slope of the pressure drop curve.

Table 5.2 – Experimental measurements.

ΔP_{exp} **(Pa)**	$\dot{m}_l$ **(Kg/h)**	$\bar{V}$ **(m/s)**	T_{in} **(°C)**	T_{out} **(°C)**
2353	530.5	0.0648	24.9	25.1
2387	671.4	0.0820	24.8	24.9
2535	1026.6	0.1254	24.4	24.6
2669	1382.5	0.1689	25.3	25.3
2770	1747.8	0.2135	25.5	25.4
2947	2097.2	0.2562	25.1	25.2

Figure 5.2 – Experimental pressure drop versus mean velocity. Error bars indicate the accuracy of the sensor (60 Pa).

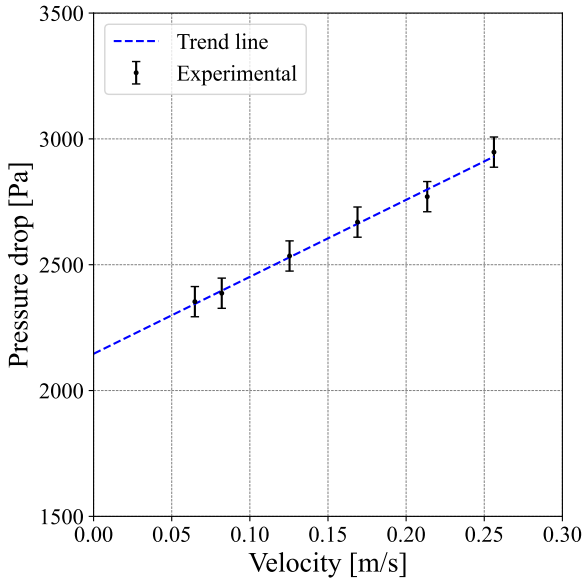

5.1.1 Experimental friction factor

The experimental friction factor (f_{exp}) was calculated using the data measured during the test (ΔP_{exp}, ρ, and $\bar{V}$) and the dimensions of the test section (D and L) by the Fanning

equation (Equation 3.9). This experimental values served as a reference for comparison with the analytical friction factors values calculated with different correlations, which will be presented in the subsequent steps. The results were plotted as a function of the Reynolds number of Metzner and Reed for Power Law fluids, as illustrated in Figure 5.3 and detailed in Table 5.3.

Figure 5.3 – Variation of experimental friction factor respect the Reynolds number for Power Law fluids of Metzner e Reed (1955).

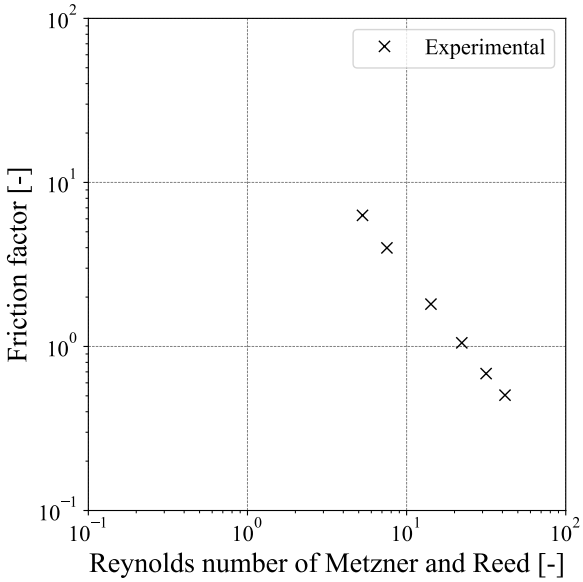

Table 5.3 – Experimental Fanning friction factor calculation.

ΔP_{exp} **(Pa)**	ρ **(Kg/m^3)**	$\bar{V}$ **(m/s)**	D **(m)**	L **(m)**	f_{exp} **(-)**
2353	998	0.0648	0.0539	2.4	6.2984
2387	998	0.0820	0.0539	2.4	3.9893
2535	998	0.1254	0.0539	2.4	1.8121
2669	998	0.1689	0.0539	2.4	1.0521
2770	998	0.2135	0.0539	2.4	0.6833
2947	998	0.2562	0.0539	2.4	0.5049

As previously mentioned, the pressure drop in a flow system is proportional to the flow velocity, but inversely proportional to the friction factor. In the laminar flow of a non-Newtonian fluid, the friction factor also varies inversely with the Reynolds number, which depends on velocity. Given that velocity is the primary factor affecting the friction factor and the pressure drop, the observed decreasing in friction factor with flow velocity during the experiment aligns well with theoretical predictions. This confirms that the experimental friction factor behaved as expected.

5.1.2 Calculation of the Reynolds number models

The behavior of the Reynolds numbers, calculated for the experimental conditions studied using the models described in Section 3.1, resulted in different values for the same mean flow velocity ($\bar{V}$), as demonstrated in Table 5.4.

Table 5.4 – Reynolds number for each mean flow velocity using different models developed for Herschel-Bulkley and Power Law fluids.

$\bar{V}$ (m/s)	$N_{\text{Re, Metzner(PL)}}$ (-)	$N_{\text{Re, Metzner(B)}}$ (-)	$N_{\text{Re, Slatter}}$ (-)	$N_{\text{Re, Güzel}}$ (-)	$N_{\text{Re, Madlener}}$ (-)
0.0648	5.3	1.2	2.5	0.9	2.2
0.0820	7.5	1.8	3.8	1.4	3.3
0.1254	14.2	3.4	8.1	3.1	6.9
0.1689	22.2	5.3	13.5	5.4	11.7
0.2135	31.6	7.5	20.3	8.3	17.5
0.2562	41.5	9.8	27.6	11.6	23.9

The values presented in Table 5.4 are plotted in Figure 5.4, and it is observed that the outcomes obtained with the Güzel *et al.* (2009b) model ($N_{\text{Re,Güzel}}$) are significantly lower compared to those obtained using the Reynolds number for Power Law fluids of Metzner e Reed (1955) ($N_{\text{Re, Metzner (PL)}}$), but very similar to those calculated with the Reynolds number for Bingham fluids of Metzner (1957) ($N_{\text{Re, Metzner (B)}}$). The relationship of inertial and viscous forces proposed by Slatter (1995) ($N_{\text{Re,Slatter}}$) and Madlener *et al.* (2009) ($N_{\text{Re,Madlener}}$) yielded intermediate values.

Figure 5.4 – Reynolds numbers for the working fluid with $\rho = 998$ kg/m^3, $\tau_0^H = 7.67$ Pa, $n = 0.5$ and $k = 1.83$ Pa.s^n.

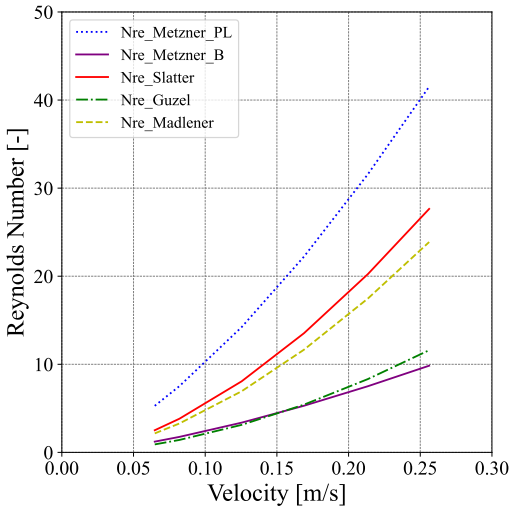

The differences between the trend curves of the various Reynolds number models presented in Figure 5.4 may be attributed to the consideration of yield stress in their calculations. The Reynolds numbers introduced by Metzner (1957), Slatter (1995), Madlener *et al.* (2009), and Güzel *et al.* (2009b) incorporate yield stress either implicitly or explicitly, whereas the Reynolds number for Power Law (PL) fluids of Metzner e Reed (1955) does not. This distinction likely accounts for the observed variations among the models.

To plot the influence of yield stress on the Reynolds number, two hypothetical cases were considered as depicted in Figure 5.5. From these two cases, it can be concluded that a higher yield stress value is associated with a lower Reynolds number when applied the Metzner (B), Slatter, Madlener and Güzel model, due to the yield stress variable is in the denominator. It is important to reiterate that this conclusion does not apply to the Reynolds number of Metzner and Reed (PL), as it remained unchanged in both hypothetical cases because this model does not consider yield stress in its calculation, a defining characteristic of viscoplastic fluids.

Figure 5.5 – Influence of yield stress (τ_0^H) on the Reynolds number.

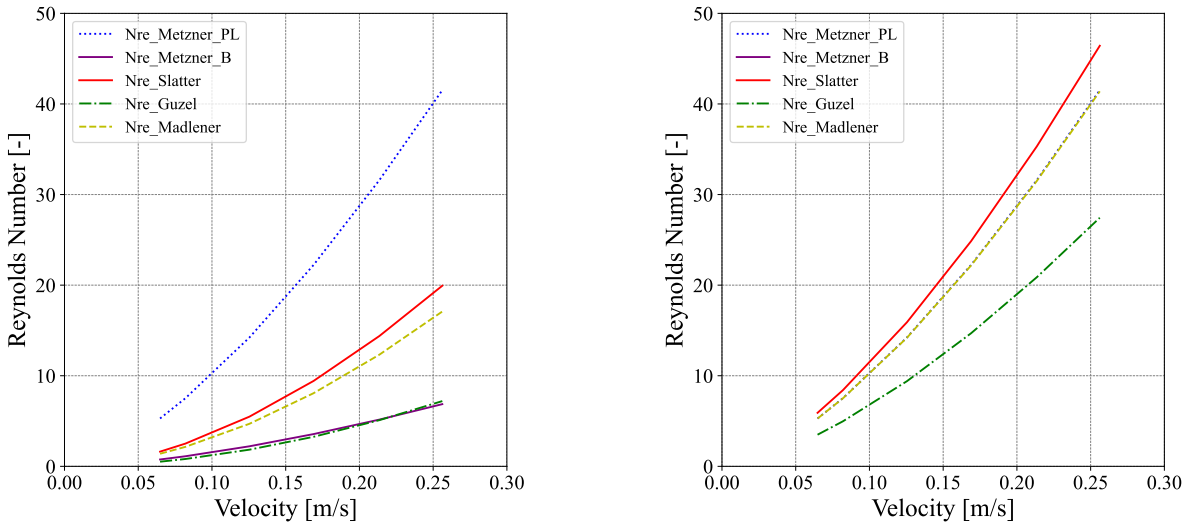

(a) $n = 0.5$, $k = 7.76$ Pa.s^n, $\tau_0^H = 15$ Pa.

(b) $n = 0.5$, $k = 7.76$ Pa.s^n, $\tau_0^H = 10^{-5}$ Pa.

As a final analysis of this section, it is important to highlight the significance of observing the trend curves of the different Reynolds number models, as the choice of friction factor correlation to use depends on the Reynolds number value, and it could be critical in cases where the flow velocity range approaches the transition region. In such cases, one model might identify the flow regime as completely laminar, while another might define it as turbulent. Matoba *et al.* (2023) quantified the significant influence of the Reynolds number in estimating the friction factor, which has an impact of $25.52\,\%$.

5.1.3 Prediction of pressure drop using recommended friction factor-Reynolds number combinations from literature

In this step, the analytical pressure drops were initially computed using the friction factor correlations of Hanks (1978), Güzel *et al.* (2009b), and Swamee e Aggarwal (2011) with the Reynolds numbers recommended by each author (see description of each correlation in Section 3.2) in order to assess their predictive capability. Results are plotted in Figure 5.6:

Figure 5.6 – Comparison of analytical pressure drop calculated using Hanks, Swamee, and Güzel correlations with their recommended Reynolds numbers. Error bars indicate the accuracy of the sensor (60 Pa).

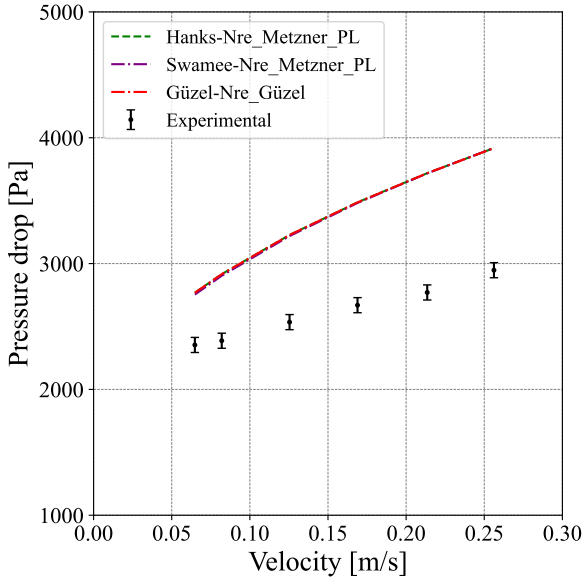

The models did not accurately reflect the experimental data in terms of velocity. However, the behavior of the models and the data is consistent. The trend of increasing pressure drop with increasing velocity, while decreasing slope of the pressure drop curve, is observed in all correlations and is consistent with the shear-thinning behavior of Herschel-Bulkley fluids.

5.1.4 Performance metrics of analytical pressure drop

The three correlations and their respective Reynolds numbers collectively overestimated the predicted pressure drop by $\sim 27.4\%$ compared to the experimental values, as presented in Table 5.5. Therefore, in the next steps, a combinatorial analysis of friction factor correlations and Reynolds number models was carried out in an attempt to approximate the analytical results to the experimental pressure drops.

Table 5.5 – Evaluation of Mean Absolute Error (MAE) and Mean Absolute Percentage Error (MAPE) for Friction factor and its recommended Reynolds number models compared to experimental data.

Combination used to calculate ΔP_c	**MAE**	**MAPE**
Friction factor of Hanks + Reynolds number of Metzner and Reed (PL)	729 Pa	27.49%
Friction factor of Swamee + Reynolds number of Metzner and Reed (PL)	722 Pa	27.20%
Friction factor of Güzel + Reynolds number of Güzel	729 Pa	27.49%

5.2 Combinatorial analysis and comparative evaluation of predicted results with experimental data

Considering that the five models for the Reynolds number gave different results (as observed in Figure 5.4 and discussed in Section 5.1.2), their effects on the friction factor calculation were evaluated, even if they are not recommended by the authors. Hence, friction factor correlations were computed for each Reynolds number model to determine the best possible friction factor-Reynolds number combination. In addition, the Fanning friction factor for Newtonian fluids (Equation 3.8) was considered as another relevant parameter in the combinations.

Then, the pressure drops estimated with the friction factor-Reynolds number combinations were compared with the results of the friction factor-independent pressure drop equations, formulated by Metzner e Reed (1955) (Equation 3.13) and Chhabra e Richardson (2011) (Equation 3.17), following the chart indicated in Figure 5.7.

The outcomes of the new friction factor-Reynolds number combinations suggested in Figure 5.7 are shown in Figure 5.8. The mean percentage deviations (MAPE) between the calculated results using the combinations and the experimental data is provided in Table 5.5.

Figure 5.7 – Schematic of pressure drop calculation combining the friction factor correlations with each possible Reynolds number model.

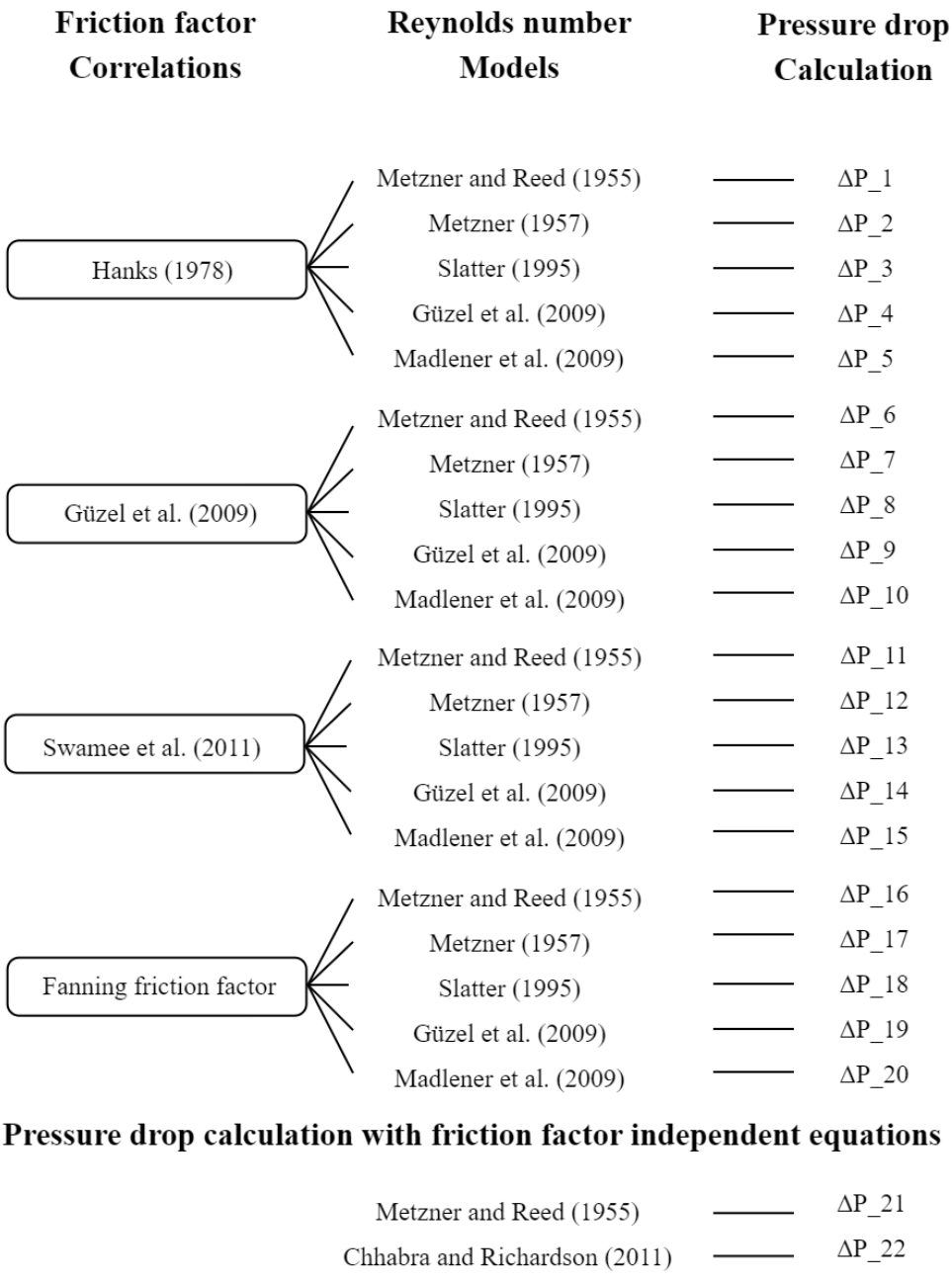

Figure 5.8 – Comparison of friction factor values computed with different correlations for a consistent Reynolds Number.

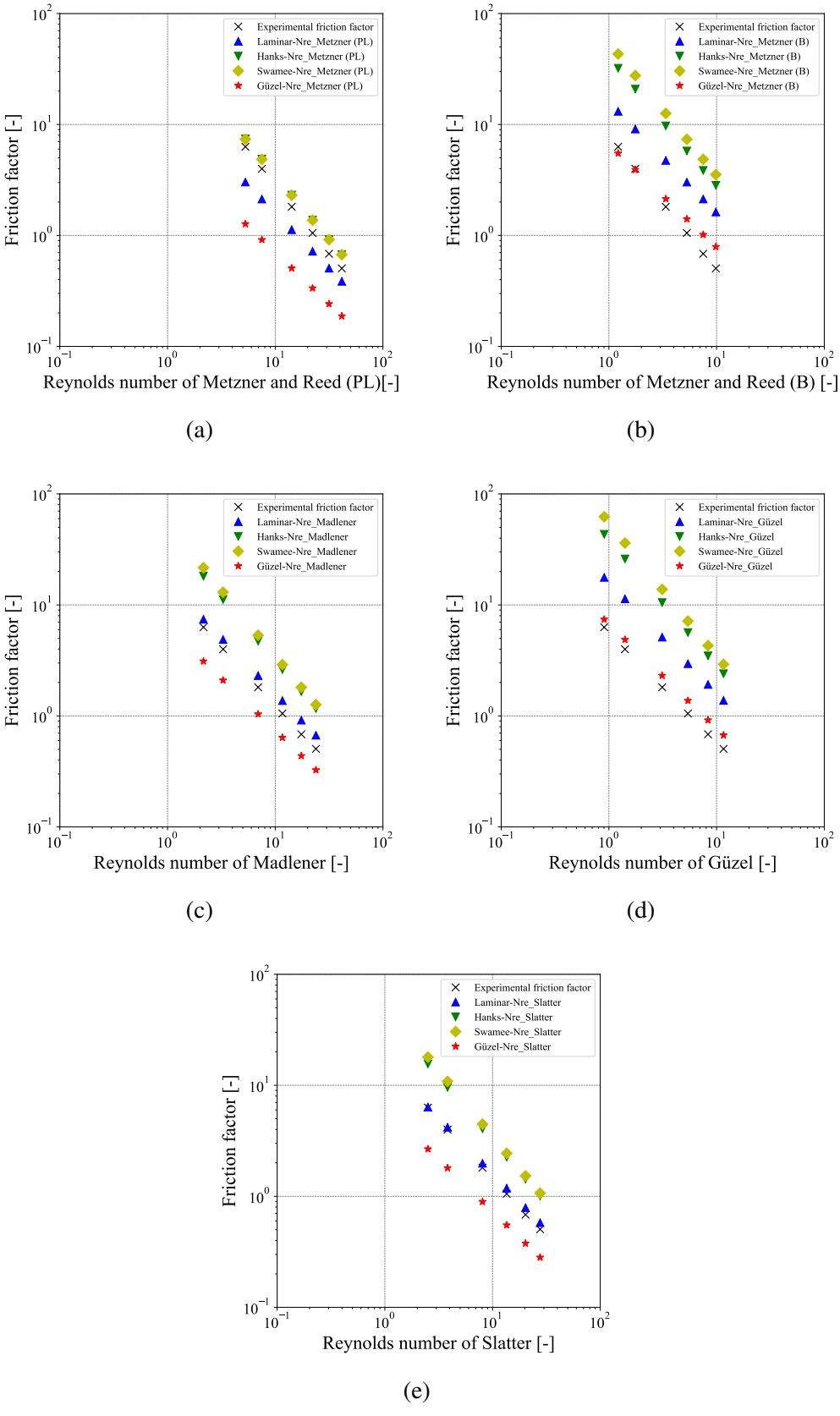

5.2.1 Analysis of friction factor and Reynolds numbers combinations

Results in Table 5.6 made it evident that, neither Hanks and Güzel model nor the Swamee model demonstrated any improvements in their results by employing different Reynolds number. However, the correlation of the friction factor for the laminar flow regime of Newtonian fluids along with the Reynolds number of Slatter yields more approximate results compared to the experimental data, with a MAPE of 9.71%.

Table 5.6 – Evaluation of Mean Absolute Percentage Error (MAPE) for Friction factor-Reynolds number combinations compared to experimental data.

Reynolds number model	**Friction factor correlation**			
	Hanks	**Swamee**	**Guzel**	**Newtonian**
Metzner and Reed (PL)	27.49 %	27.20 %	70.77 %	36.27 %
Metzner (B)	440.43 %	597.21 %	28.60 %	169.86 %
Slatter	122.67 %	145.05 %	49.99 %	9.71 %
Guzel	474.18 %	657.28 %	27.49 %	180.50 %
Madlener	158.72 %	192.48 %	41.92 %	27.43 %

In the case of the Hanks and Swamee correlations, one could hypothesize that their best performance with the Metzner and Reed (PL) Reynolds number, which has the most extensive range of values as seen in Figure 5.4, suggests that using another Reynolds number with a more restricted range of values would result in overestimated friction factors. This is due to the inverse relationship between the Reynolds number and the friction factor. Moreover, findings showed that the friction factor correlations of Hanks and Swamee are quite comparable to each other, as long as the same Reynolds number model is used in both correlations. This is because the Swamee correlation is essentially an explicit approximation of the Hanks correlation, with the only difference being that the Swamee correlation is not affected by the ϕ value (determined by iterative methods applying Equation 2.18), unlike the Hanks correlation.

For the Güzel correlation, an opposite effect to that of the Hanks and Swamee correlations is observed. Its best performance is achieved with Reynolds numbers that provide a more limited range of values, such as the Reynolds number for Bingham (B) fluids of Metzner or Güzel's own Reynolds number.

According to Table 5.6, the combinations with the lowest percentage deviation with respect to the experimental friction factor were:

- Friction factor for laminar flow regime of Newtonian fluids + Reynolds number of Slatter (MAPE = 9.71%).

- Friction factor of Swamee + Reynolds number of Metzner and Reed (PL) (MAPE = 27.20%).
- Friction factor for laminar flow of Newtonian fluids + Reynolds number of Madlener (MAPE = 27.43%).
- Friction factor of Hanks + Reynolds number of Metzner and Reed (PL) (MAPE = 27.49%).
- Friction factor of Güzel + Reynolds number of Güzel (MAPE = 27.49%).
- Friction factor of Güzel + Reynolds number of Metzner (B) (MAPE = 28.60%).

5.2.2 Calculation of pressure drop using the best combinations of friction factor and Reynolds number

Figure 5.9 presents the predicted pressure drop results calculated using the Fanning equation (Equation 3.9) with the best friction factor-Reynolds numbers combinations observed in Figure 5.8, and detailed in Table 5.6. The results were compared with the calculated pressure drops using equations that do not depend on the friction factor, as given by Equation 3.13 from Metzner e Reed (1955) and Equation 3.17 from Chhabra e Richardson (2011), as well as with the experimental pressure drop.

Figure 5.9 – Comparison of pressure drop trends calculated with the best friction factor and Reynolds number combinations from the results shown in Figure 5.8.

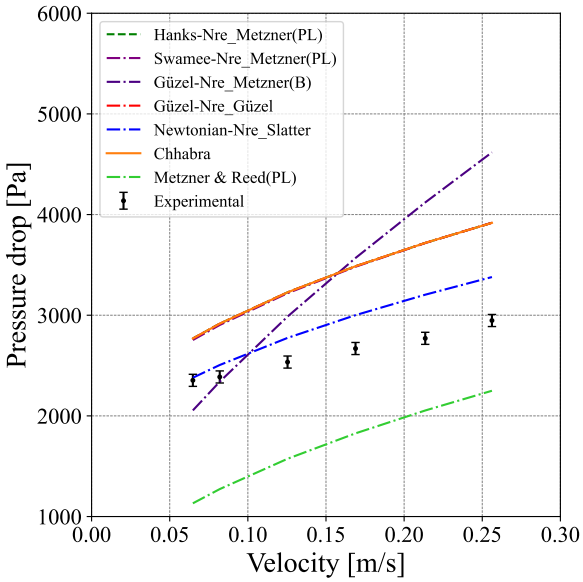

The pressure drop trends using the best friction factor-Reynolds number combinations show visual coherence with the friction factor behavior observed in Figure 5.8.

For pressure drops calculated by combining the Güzel correlation with the Güzel Reynolds number, as well as the pressure drop calculated by combining the correlations of Hanks and Swamee, with the Reynolds number of Metzner and Reed (PL), yielded consistent results with the Chhabra and Richardson pressure drop equation.

On the other hand, although Table 5.6 showed that the combination of the Güzel correlation with the Reynolds number of Metzner (B) had a similar MAPE to the combination of the Güzel correlation with the Reynolds number of Güzel, the pressure drops calculated with Güzel-Metzner (B) combination showed a marked tendency to overestimate the values compared to the pressure drops calculated with Güzel-Güzel combination.

5.2.3 Statistical analysis of the pressure drop results from combinatorial analysis

The pressure drop calculations using the Fanning equation with the friction factor correlation for Newtonian fluids and the Reynolds number of Slatter exhibited lower errors compared to experimental pressure drops, yielding an average error magnitude of $264\,\text{Pa}$, as indicated in Table 5.7. This combination gave even better results than those obtained using the friction factor correlations (Hanks, Swamee, and Güzel) or pressure drop equations (Chhabra and Richardson) explicitly developed for viscoplastic fluids and satisfactorily captured the variation of the pressure drop curve, as illustrated in Figure 5.9.

Table 5.7 – Evaluation of Mean Absolute Error in predicted pressure drop.

	Pressure Drop Equations					
Reynolds Numbers Models	**Metzner and Reed (PL) [Pa]**	**Chhabra [Pa]**	**from Fanning equation [Pa]**			
			Hanks	**Swamee**	**Güzel**	**Newtonian**
-	926	729	-	-	-	-
Metzner and Reed (PL)	-	-	729	722	1835	926
Metzner (B)	-	-	11536	15602	786	4520
Slatter	-	-	3167	3733	1295	264
Güzel	-	-	12197	16860	729	4706
Madlener	-	-	4101	4957	1083	727

It is also worth mentioning that the similarity in the results obtained when calculating the pressure drop using the correlation for laminar flow of Newtonian fluids (Equation 3.8) along with the Reynolds number of Metzner and Reed for Power Law fluids (Equation 3.1 and 3.2), and those calculated with the pressure drop equation of Metzner and Reed (PL) (Equations 3.13 and 3.2) may not be entirely unexpected. It is crucial to remember that Metzner e Reed (1955) incorporated the correlation for laminar flow of Newtonian fluids in developing the Generalized Reynolds number (Equation 3.1), from which they derived their pressure drop equation for laminar regime.

Analyzing the mean absolute errors in percentage terms, as stated in Table 5.8, reveals that the predicted pressure drop values using the friction factor correlation for Newtonian fluids with the Reynolds number of Slatter exhibit a $9.71\,\%$ deviation from the measured data.

Table 5.8 – Evaluation of Mean Absolute Percentage Error in predicted pressure drop.

	Pressure Drop Equations					
Reynolds Numbers Models	**Metzner and Reed [Pa]**	**Chhabra [Pa]**	**from Fanning equation [Pa]**			
			Hanks	**Swamee**	**Güzel**	**Newtonian**
-	36.27 %	27.49 %	-	-	-	-
Metzner and Reed (PL)	-	-	27.49 %	27.20 %	70.77 %	36.27 %
Metzner (B)	-	-	440.43 %	597.21 %	28.60 %	169.86 %
Slatter	-	-	122.67 %	145.05 %	49.99 %	9.71 %
Güzel	-	-	473.18 %	657.28 %	27.49 %	180.50 %
Madlener	-	-	158.72 %	192.48 %	41.92 %	27.43 %

Moreover, $50\,\%$ of the predicted values fall within a $\pm 10\,\%$ tolerance of the experimental data (Figure 5.10a). However, when considering a $\pm 30\,\%$ tolerance, $100\,\%$ of the predicted data falls within the range (Figure 5.10b). On the other hand, when the same correlation for Newtonian fluids is combined with the Reynolds number of Madlener, it presents a mean deviation of $27.43\,\%$ in relation to the experimental pressure drop.

Figure 5.10 – Pressure drop comparison: Measured values vs Predicted values.

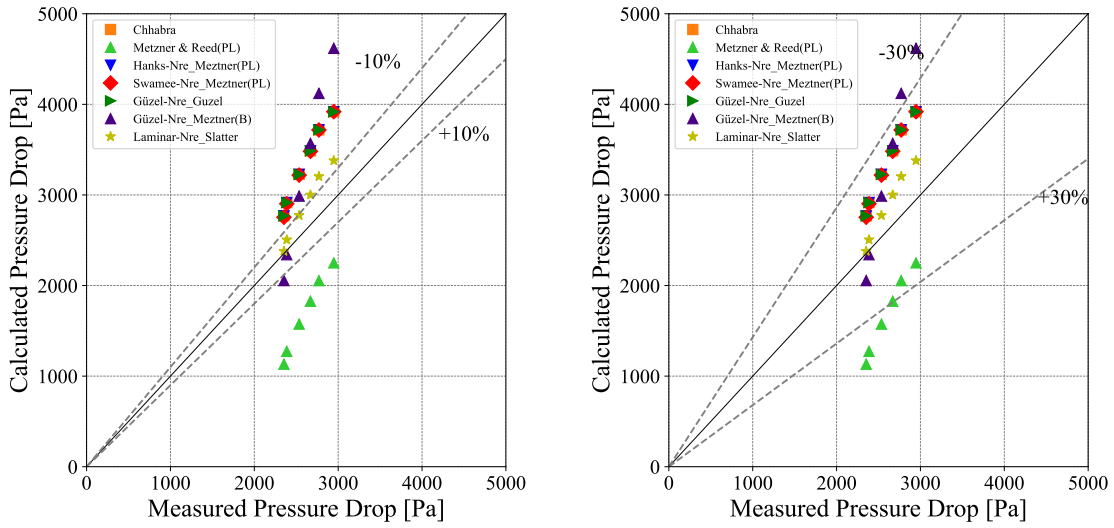

(a) (b)

About the pressure drop equation developed for viscoplastic fluids by Chhabra and Richardson, no predicted values were observed to agree with a tolerance of $\pm 10\,\%$, yet $100\,\%$ of the results fall inside the $\pm 30\,\%$ tolerance.

The results obtained with the Metzner and Reed (PL) equation also did not show predicted values within the tolerance range of $\pm 10\,\%$. However, $30\,\%$ of the values fall within

the $\pm 30\,\%$ tolerance threshold.

Lastly, when using the Fanning equation with the correlations of Hanks and Swamee, as well as the correlation for laminar flow of Newtonian fluids combined with the Reynolds number of Güzel, the predictions for pressure drops are less accurate.

In summary, after observing the trend curves of pressure drops, MAE and MAPE, the best pressure drop forecasts were obtained with the following combinations:

- Friction factor for laminar flow regime of Newtonian fluids + Reynolds number of Slatter (MAPE = 9.71%).
- Friction factor of Swamee + Reynolds number of Metzner and Reed (PL) (MAPE = 27.20%).
- Friction factor for laminar flow of Newtonian fluids + Reynolds number of Madlener (MAPE = 27.43%).
- Friction factor of Hanks + Reynolds number of Metzner and Reed (PL) (MAPE = 27.49%).
- Friction factor of Güzel + Reynolds number of Güzel (MAPE = 27.49%).
- Pressure drop equation of Chhabra and Richardson (MAPE = 27.49%).
- Pressure drop equation of Metzner and Reed (PL) (MAPE = 36.27%).

The pressure drop calculated using the combination of the Güzel correlation and the Reynolds number of Metzner (B), despite presenting a MAPE of 28.60%, was not considered a good approximation because of the calculated pressure drop curve has a steeper slope than the experimental one, as observed in Figure 5.9. In other words, the trend of the model curve and the experimental data do not exhibit the same behavior. This discrepancy demonstrated a tendency to further overestimate the pressure drop values at velocities higher than those used in the experiment of this study.

5.3 Comparison of combinatorial analyzes with literature data

Comparison was carried out using experimental data collected by other researchers in similar studies. The objective was to evaluate the combinations of friction factor correlations and Reynolds number models that provided the closest predictions respect the experimental pressure drops of this study, as summarized in Section 5.2.3.

According to the information provided in Tables 5.7 and 5.8, it was observed that the following combinations showed remarkably similar results among themselves:

- Friction factor of Swamee + Reynolds number of Metzner and Reed (PL).
- Friction factor for laminar flow of Newtonian fluids + Reynolds number of Madlener.
- Friction factor of Hanks + Reynolds number of Metzner and Reed (PL).
- Friction factor of Güzel + Reynolds number of Güzel.
- Pressure drop equation of Chhabra and Richardson.

Therefore, among these options, the Güzel combination, developed based on Carbopol experiments, was selected for comparison with literature data.

Additionally, the combinations with the best results, i.e., the friction factor for laminar flow of Newtonian fluids along with Reynolds number of Slatter, and the pressure drop equation for Power Law fluids of Metzner and Reed, both developed analytically, were included.

5.3.1 Fluids reported in the literature

Eight Herschel-Bulkley fluids composed of Carbopol 940 and 980 were selected for this comparison.

- Fluids 1 to 4 were sourced from the work of Güzel *et al.* (2009a). The experiments were conducted in a flow loop with an internal diameter of 0.0508 m and a test section of 10 m. The rheological characterization was performed at the same temperature as the samples taken during the experimental tests, ranging from 29 to 35 °C.
- Fluid 5 comes from the research of Magnon e Cayeux (2021). The experimental setup consisted of a glass tube with an internal diameter of 0.0155 m and a test section of 4.83 m. The experimental tests were conducted at an average temperature of 27.9 °C.
- Fluids 6 to 8 were taken from the Abou-Kassem *et al.* (2023) study. The pressure drop was measured in a borosilicate glass flow line with an internal diameter of 0.095 m, a length of 3.08 m, and a stabilized flow loop temperature of 30 °C.

The rheological properties for fluids 1 to 8 measured by the authors of each study are listed in Table 5.9:

Table 5.9 – Rheological characteristics of Herschel-Bulkley fluids employed in experimental tests by (a) Güzel *et al.* (2009a), (b) Magnon e Cayeux (2021) , and (c) Abou-Kassem *et al.* (2023).

Fluid	**Aqueous solution**	**Polymer concentration (wt.%)**	τ_0^H **(Pa)**	n **(-)**	k **(Pa.s^n)**	ρ **(kg/m^3)**	**Pipe inner diameter (m)**
Fluid 1[a]	Carbopol 940	0.15	5.60 - 6.00	0.37 - 0.46	2.87 - 4.79	998	0.0508
Fluid 2[a]	Carbopol 940	0.10	0.95 - 1.80	0.50 - 0.54	0.60 - 1.11	998	
Fluid 3[a]	Carbopol 940	0.10	1.20 - 2.00	0.36 - 0.53	0.92 - 2.05	998	
Fluid 4[a]	Carbopol 940	0.075	0.28 - 0.38	0.58 - 0.61	0.26 - 0.37	998	
Fluid 5[b]	Carbopol 980	Unspecified	0.909	0.641	0.272	997	0.0155
Fluid 6[c]	Carbopol 940	0.07	2.56	0.71	0.33	997	0.095
Fluid 7[c]	Carbopol 940	0.06	0.92	0.59	0.39	997	
Fluid 8[c]	Carbopol 940	0.045	0.15	0.73	0.04	997	

5.3.2 Experimental data of Güzel, Frigaard and Martinez - Fluids 1 to 4

Using the experimental data of Güzel, and contrasting it with the analysis of the information generated for this study (Section 5.2), the friction factor correlation of Güzel along with the Reynolds number proposed by the same author (hereinafter referred to as: Combination 1) provided the closest pressure drop predictions to the measured pressure drops for fluids 1 to 4 (Figure 5.11). A 10% error bar was added to the experimental points in the figures to facilitate visual comparison between the analytical and experimental data sets.

Figure 5.11 – Pressure drop predictions for fluids 1 to 4 from Güzel *et al.* (2009a) experimental data set.

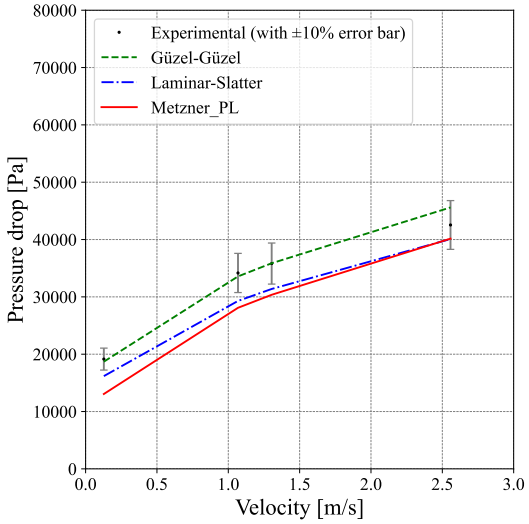

(a) Fluid 1

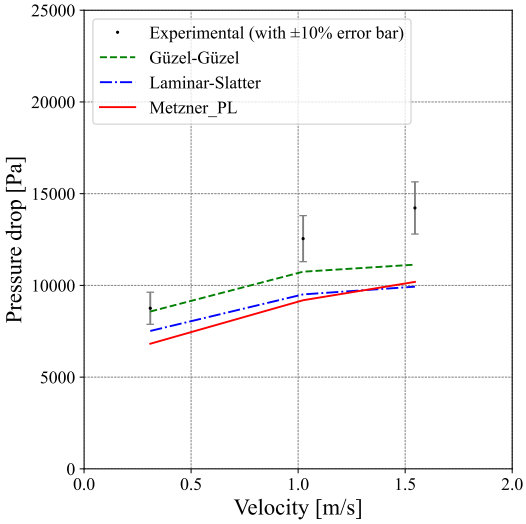

(b) Fluid 2

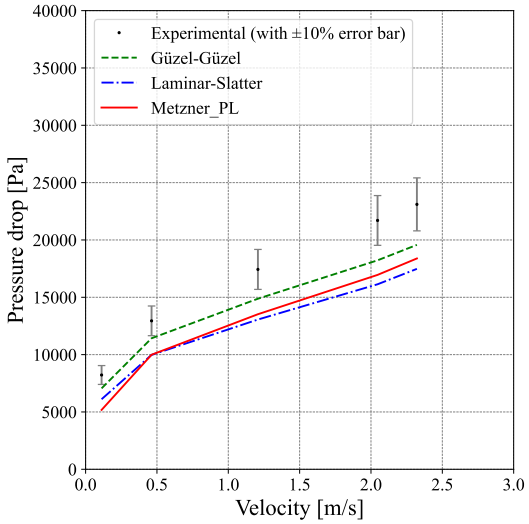

(c) Fluid 3

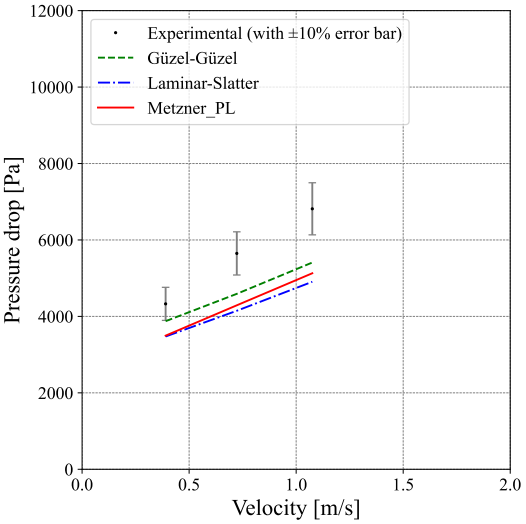

(d) Fluid 4

The good performance of Combination 1 was expected since Güzel developed his

equations based on the same four experimental data. The best approximation achieved by Combination 1 was observed for fluid 1, with an average percentage deviation of 2.87%.

Regarding the combination of the friction factor correlation for Newtonian fluids in laminar regime with the Reynolds number of Slatter (from now on referred to as: Combination 2) and the pressure drop equation of Metzner and Reed (PL), although they did not demonstrate predictive capability as close as Combination 1, both combinations showed a percentage deviation of less than 25.73% for fluids 1 to 4. This value is quite close to the percentage deviation of $\sim 27.4\%$ obtained by the Metzner and Reed (PL) equation and the combinations evaluated in Section 5.2.3, relative to the experimental data of this study.

According to Güzel *et al.* (2009a), discrepancies between experimental and predicted pressure drop or friction factor values could be attributed to variations in the parameters n and ϕ during the experimental test. These parameters, he noted, are sensitive to viscous heating and fluid deterioration. Therefore, he argued that it would not be possible to fit experimental data to a theoretical curve for the friction factor of non-Newtonian fluids, including his own friction factor correlation.

The variations in rheological properties for fluids 1 to 4 during the Güzel's experiments are detailed in Appendix D. The average percentage deviations (MAPE) for each combination are detailed in Table 5.10.

Table 5.10 – Evaluation of Mean Absolute Percentage Error (MAPE) for fluids 1, 2, 3, and 4 from Güzel *et al.* (2009a).

	MAPE			
Combination	**Fluid 1**	**Fluid 2**	**Fluid 3**	**Fluid 4**
Güzel-Güzel	2.87 %	12.71 %	14.38 %	16.61 %
Laminar-Slatter	11.98 %	22.84 %	24.74 %	24.77 %
Metzner and Reed	17.59 %	25.73 %	24.92 %	22.67 %

5.3.3 Experimental data of Magnon and Cayeux - Fluid 5

Figure 5.12 presents the predicted pressure drop curves calculated by Combination 1 (Güzel-Güzel), Combination 2 (Laminar-Slatter), and the pressure drop equation of Metzner and Reed (PL), and in Table 5.11, the MAPE results for each combination are shown.

The trend curves of all combination fell within the $10\,\%$ error bars. Nonetheless, it was observed that the closest matching results, computed by the Metzner and Reed (PL) equation, had a deviation of $11.24\,\%$.

Figure 5.12 – Pressure drop prediction for fluid 5 from Magnon e Cayeux (2021) experimental data set.

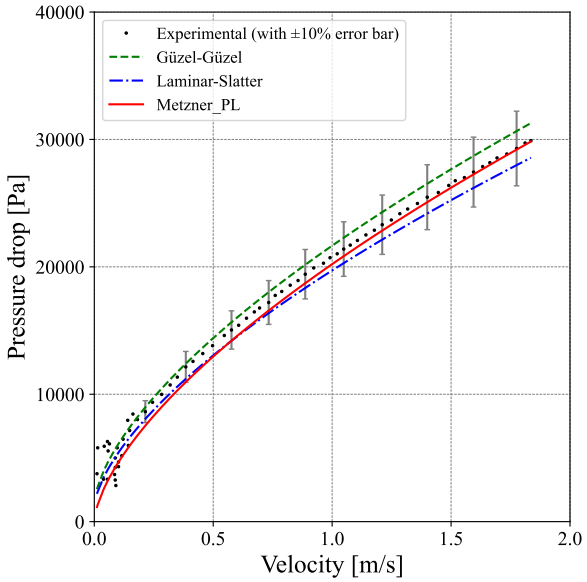

Table 5.11 – Evaluation of Mean Absolute Percentage Error (MAPE) for fluid 5 from Magnon e Cayeux (2021).

Combination	**MAPE**
Güzel-Güzel	12.11 %
Laminar-Slatter	11.74 %
Metzner and Reed (PL)	11.24 %

The MAPE performance metric could be affected by the high dispersion of points (pressure drops) recorded at velocities lower than 0.2 m/s. If these outlier points are disregarded, the percentage deviation for Combination 1 (Güzel-Güzel), Combination 2 (Laminar-Slatter), and the Metzner and Reed (PL) equation improves significantly, as indicated in Table 5.12:

Table 5.12 – Evaluation of Mean Absolute Percentage Error (MAPE) for fluid 5 from Magnon e Cayeux (2021) disregarding outlier points.

Combination	**MAPE**
Güzel-Güzel	4.14 %
Laminar-Slatter	5.33 %
Metzner and Reed (PL)	3.77 %

Although Combination 2 was not the closest to the experimental data, it shows a deviation percentage as low as that of Combination 1 and the Metzner and Reed (PL) equation. This low MAPE value could be attributed to the high density of points measured by Magnon

and Cayeux during the experimental test, which reduces the impact of outlier points on the performance metrics calculation and improve the representativeness of the collected points in relation to the behavior of the system, achieving better agreement between the experimental and analytical data.

5.3.4 Experimental data of Abou-Kassem, Bizhani and Kuru - Fluids 6 to 8

Figure 5.13 and 5.14 shows the experimental data for fluids 6 and 7 from Abou-Kassem's work, compared with the pressure drop predictions calculated using the three combinations. The percentage deviations are presented in Tables 5.13 and 5.14.

Figure 5.13 – Pressure drop predictions for fluid 6 from Abou-Kassem *et al.* (2023) experimental data set.

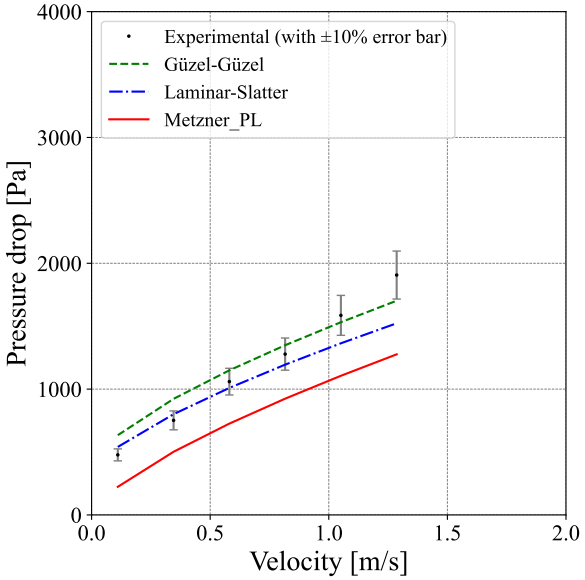

Table 5.13 – Evaluation of Mean Absolute Percentage Error (MAPE) for fluid 6 from Abou-Kassem *et al.* (2023).

Combination	**MAPE**
Güzel-Güzel	13.95 %
Laminar-Slatter	10.86 %
Metzner and Reed (PL)	34.82 %

According to Abou-Kassem, the Hanks correlation provided the best analytical results in the laminar regime compared to his experimental data. In this study, Combination 1 can be used as a reference since it gives similar outcomes to the Hanks correlation, as demonstrated in Section 5.2.3.

Figure 5.14 – Pressure drop predictions for fluid 7 from Abou-Kassem *et al.* (2023) experimental data set.

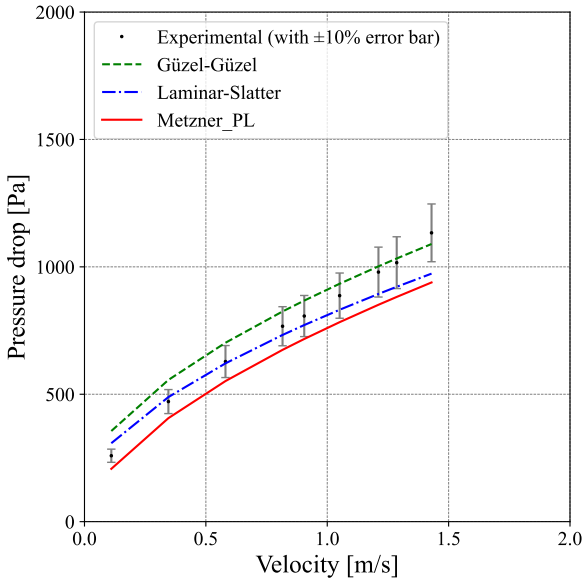

Table 5.14 – Evaluation of Mean Absolute Percentage Error (MAPE) for fluid 7 from Abou-Kassem *et al.* (2023).

Combination	**MAPE**
Güzel-Güzel	10.60 %
Laminar-Slatter	7.90 %
Metzner and Reed (PL)	13.81 %

For these fluids 6 and 7, although Combination 2 did not achieve as low a MAPE as it did for fluid 5, it outperformed Combination 1 and Metzner and Reed (PL) equation as the best approximation for fluid 6, with a deviation of 10.86 %, and fluid 7, with 7.90 %. These values are relatively close to the MAPE of 9.71 % identified with the experimental data from this study. Although its predictive capacity is not fixed percentage-wise and the MAPEs varied among fluids 5, 6, and 7, the differences are not large, and the values are close to each other within a reasonable error range. This could indicate that Combination 2 is reliable for different rheological characteristics.

Lastly, Figure 5.15 shows the pressure drop curves for fluid 8, and Table 5.15 details the percentage deviation from the experimental data.

In this particular case, the Metzner and Reed (PL) pressure drop equation provided the best approximation compared to Combination 1 and Combination 2, whose results were exceptionally high in relation to the first seven fluids evaluated, with deviations exceeding 40 %.

Figure 5.15 – Pressure drop prediction for fluid 8 characterized by Abou-Kassem *et al.* (2023) experimental data set.

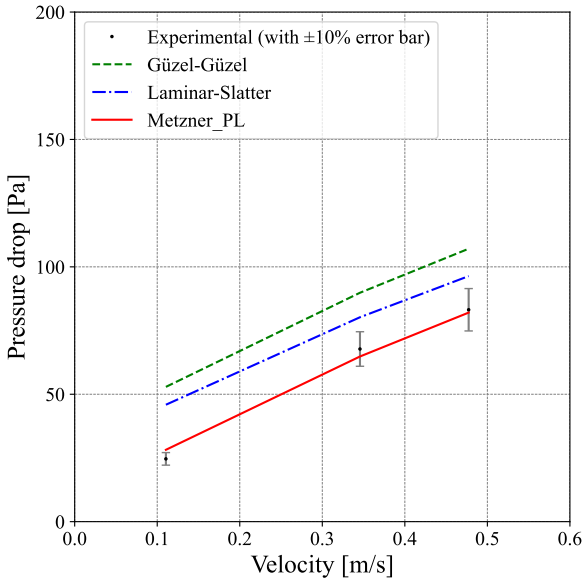

Table 5.15 – Evaluation of Mean Absolute Percentage Error (MAPE) for fluid 8 from Abou-Kassem *et al.* (2023).

Combination	**MAPE**
Güzel-Güzel	58.68 %
Laminar-Slatter	40.16 %
Metzner and Reed (PL)	6.70 %

This could be influenced by the rheological characteristic of the fluid, particularly its low yield stress of 0.15 Pa, which suggests that the fluid's behavior resembles that of a Power Law fluid. This characteristic may have facilitated the Metzner and Reed (PL) equation to be significantly more advantageous and accurate for this fluid, given that the Metzner and Reed (PL) equation is based on the Power Law rheological model.

Based on the experimental data from this research and the information collected from similar studies conducted by three different authors, as detailed in Table 5.9, it can be concluded that Combination 2 (Laminar-Slatter) consistently demonstrated the ability to accurately predict experimental pressure drops for a wide range of rheological parameter values within the laminar regime. These parameters include: yield stress (0.15 Pa $< \tau_0^H <$ 6 Pa), consistency index (0.04 Pa.s^n $< k <$ 4.79 Pa.s^n), Power Law index ($0.36 < n < 0.73$), and flow line diameters (0.0155 m $< D <$ 0.095 m), as can be seen in Figure 5.16, which shows an overview of the predicted data for the eight fluids used for the validation of the analysis of this study.

Figure 5.16 – Overview of the pressure drops predicted by the Laminar-Slatter and Güzel-Güzel combinations and the Metzner and Reed (PL) equation for the eight fluids used to validate the results of this study.

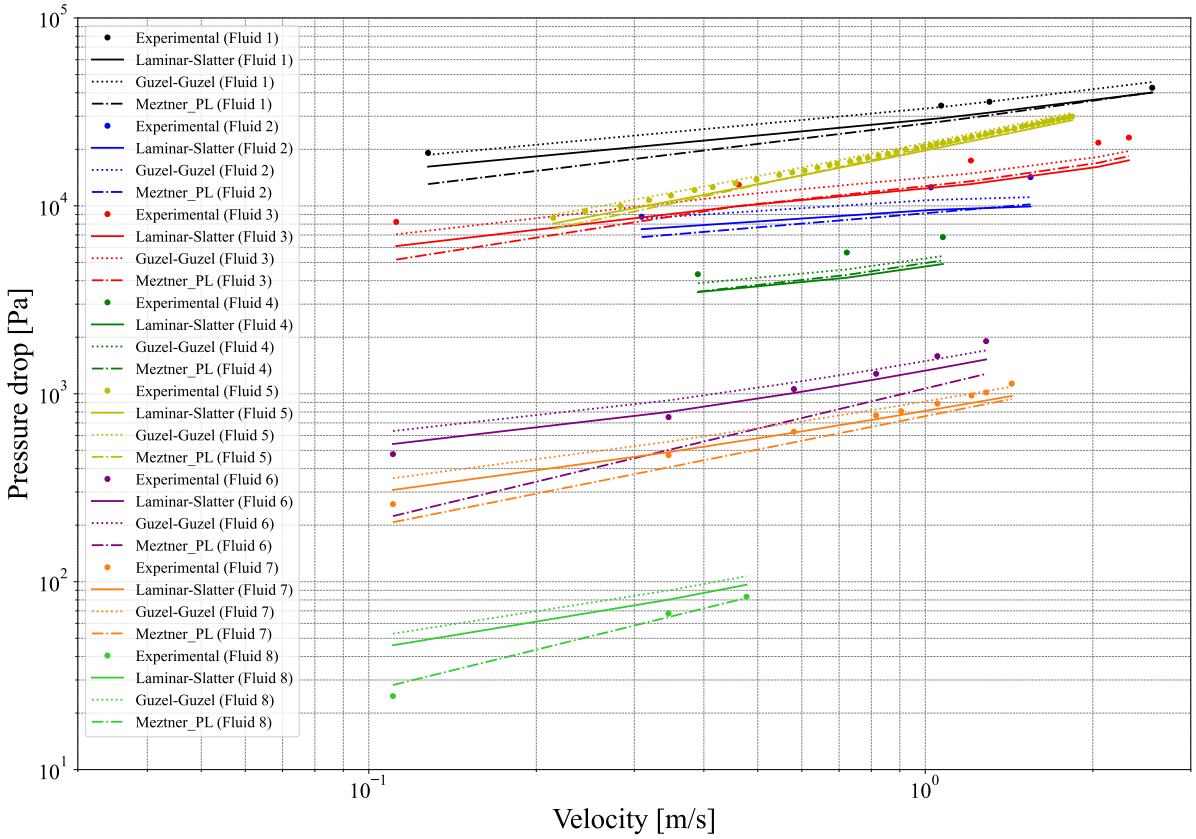

Furthermore, it is important to note that although only Güzel referred to the mechanical degradation of the fluid during the experimental test (mentioned in Section 5.3.2), none of the three referenced works mention the tolerances applied to the rheological parameters during their tests to ensure the representativeness of their measurements as was done in this study.

6 CONCLUSIONS AND RECOMMENDATIONS

6.1 Conclusions

This study conducted an experimental test under laminar and single-phase flow conditions, using a viscoplastic solution composed of Carbopol and Triethanolamine. The objective was to evaluate the capability to predict pressure drop for friction factor correlations, combined with their respective recommended Reynolds number models. The three friction factor and their Reynolds number models recommended by their authors overestimated the pressure drop values, with a mean absolute percentage error (MAPE) of $\sim 27.4\,\%$ compared to the experimental data obtained in this work.

In an attempt to bring the predicted results closer to the experimental data, a combinatorial analysis was conducted. Four friction factor correlations and five Reynolds number models, developed for viscoplastic, Power Law, and Newtonian fluids, were employed to find a possible better combination of friction factor and Reynolds number to predict the pressure drop, even though the authors had not previously recommended them in the literature. The results of the analysis showed that the friction factor correlation for Newtonian fluids in laminar flow, combined with the Reynolds number of Slatter, provides the best predictions, with a deviation of $9.27\,\%$ from the experimental data of this study.

To validate the predictive capability of the combination of the friction factor for Newtonian fluids in laminar flow with the Reynolds number of Slatter (Combination 2), experimental data from eight viscoplastic fluids from the literature were collected. These fluids have a wide yield stress (τ_0^H) range between 0.15 and 6 Pa, consistency index (k) covering 0.04 to 4.79 Pa.s^n, and Power Law index (n) varying from 0.36 to 0.73. Additionally, two other combinations that predicted the pressure drop within a tolerance of $30\,\%$ compared to the experimental data were considered: the friction factor and Reynolds number of Güzel (Combination 1) and the pressure drop equation of Metzner and Reed (PL).

Combination 1 provided predictions with deviations between $10.6\,\%$ and $58.68\,\%$ for 6 out of the 8 fluids. Its good performance with a MAPE of $4.14\,\%$ for fluid 5 was attributed to the large number of experimental points collected, which reduced the impact of outliers on the performance metric computation.

Combination 2 showed greater consistency in 4 of the 8 fluids, with a MAPE be-

tween $5.33\,\%$ and $11.98\,\%$, values relatively close to the MAPE of $9.27\,\%$ obtained from this study's experimental data. Additionally, its application is simpler than Combination 1 as it does not require iterative processes for resolution, and unlike the Metzner and Reed (PL) equation, it considers the effect of yield stress.

The Metzner and Reed (PL) equation had a MAPE between $13.81\,\%$ and $34.84\,\%$ in 6 from 8 cases. Its best results were with fluid 5, with a deviation of $3.77\,\%$, and fluid 8, with a deviation of $6.7\,\%$. The good performance with fluid 5 is justified similarly to that of Combination 1. For fluid 8, its low yield stress of only 0.15 Pa suggests it behaves like a Power Law fluid, explaining the higher accuracy of the Metzner and Reed (PL) equation with a MAPE of $6.7\,\%$.

No specific range of rheological parameter values was identified where each combination was more effective.

6.2 Recommendations for future work

Based on the above conclusions, some recommendations for future work are suggested:

1. Conduct numerical simulations to replicate the analytical results obtained in this study, using a fluid with the rheological properties of both the working fluid from this research and those extracted from the literature.

2. In this work, the generalized Reynolds number of Metzner and Reed was used to determine the flow regime of a Herschel-Bulkley fluid. However, it is emphasized that the parameter K' for Herschel-Bulkley fluids must be mathematically deduced. In the meantime, since the time available for this study was limited, the applicability of the K' parameter for Power Law and Bingham plastic fluids was used. This approached is not entirely appropriate for characterizing the flow regime of Herschel-Bulkley fluids.

3. Perform a sensitivity analysis to quantify the influence of yield stress (τ_0^H), consistency index (k), and Power Law index (n) on the Reynolds number models developed for Herschel-Bulkley fluids.

4. Extend the test matrix with various conditions of rheological properties and flow regimes to investigate the flow transition and turbulent flow regime, aiming for a comprehensive

understanding of the studied phenomenon.

BIBLIOGRAPHY

Abou-Kassem, A.; Bizhani, M.; Kuru, E. Comparative study of the accuracy of friction factor correlations developed for flow of inelastic yield power-law fluids in pipes. **Geoenergy Science and Engineering**, v. 231, p. 212346, 2023.

Alba, K.; Taghavi, S.; Bruyn, J. R. de; Frigaard, I. Incomplete fluid–fluid displacement of yield-stress fluids. part 2: Highly inclined pipes. **Journal of Non-Newtonian Fluid Mechanics**, v. 201, p. 80–93, 2013.

Bao, Y.; Zhang, J. Restart behavior of gelled waxy crude oil pipeline based on an elasto-viscoplastic thixotropic model: A numerical study. **Journal of Non-Newtonian Fluid Mechanics**, v. 284, p. 104377, 2020.

Bird, R.; Stewart, W.; Lightfoot, E. **Transport Phenomena**. Wiley, 2006. (Transport Phenomena, v. 1). ISBN 9780470115398.

Bourgoyne, A.; Millheim, K. K.; Chenevert, M. E.; Young, F. S. **Applied Drilling Engineering**. Society of Petroleum Engineers, 1986. (SPE textbook series). ISBN 9781555630010.

Caggioni, M.; Trappe, V.; Spicer, P. T. Variations of the herschel–bulkley exponent reflecting contributions of the viscous continuous phase to the shear rate-dependent stress of soft glassy materials. **Journal of Rheology**, v. 64, n. 2, p. 413–422, 2020.

Chhabra, R. P.; Richardson, J. F. **Non-Newtonian flow and Applied Rheology: engineering applications**. [S.l.]: Butterworth-Heinemann, 2011.

Chilton, R. A.; Stainsby, R. Pressure loss equations for laminar and turbulent non-newtonian pipe flow. **Journal of hydraulic engineering**, v. 124, n. 5, p. 522–529, 1998.

Curran, S.; Hayes, R.; Afacan, A.; Williams, M.; Tanguy, P. Properties of carbopol solutions as models for yield-stress fluids. **Journal of food science**, v. 67, n. 1, p. 176–180, 2002.

Dalla, L. F.; Soares, E. J.; Siqueira, R. N. Start-up of waxy crude oils in pipelines. **Journal of Non-Newtonian Fluid Mechanics**, v. 263, p. 61–68, 2019.

Fordham, E. J.; Bittleston, S. H.; Tehrani, M. A. Viscoplastic flow in centered annuli, pipes, and slots. **Industrial & engineering chemistry research**, v. 30, n. 3, p. 517–524, 1991.

Founargiotakis, K.; Kelessidis, V.; Maglione, R. Laminar, transitional and turbulent flow of herschel–bulkley fluids in concentric annulus. **The canadian journal of chemical engineering**, v. 86, n. 4, p. 676–683, 2008.

Garcia, E. J.; Steffe, J. F. Comparison of friction factor equations for non-newtoninan fluids in pipe flow. **Journal of Food Process Engineering**, v. 9, n. 2, p. 93–120, 1986.

Güzel, B.; Burghelea, T.; Frigaard, I. A.; Martinez, D. Observation of laminar–turbulent transition of a yield stress fluid in hagen–poiseuille flow. **Journal of Fluid Mechanics**, v. 627, p. 97–128, 2009.

Güzel, B.; Frigaard, I.; Martinez, D. Predicting laminar–turbulent transition in poiseuille pipe flow for non-newtonian fluids. **Chemical Engineering Science**, v. 64, n. 2, p. 254–264, 2009.

Haldenwang, R.; Sutherland, A.; Fester, V. G.; Holm, R.; Chhabra, R. Sludge pipe flow pressure drop prediction using composite power-law friction factor-reynolds number correlations based on different non-newtonian reynolds numbers. **Water Sa**, v. 38, n. 4, p. 615–622, 2012.

Hanks, R. Low reynolds number turbulent pipeline flow of pseudohomogeneous slurries. In: **Proceedings of the Hydrotransport**. [S.l.: s.n.], 1978. v. 5, p. 8–11.

Hanks, R. W. The axial laminar flow of yield-pseudoplastic fluids in a concentric annulus. **Industrial & Engineering Chemistry Process Design and Development**, v. 18, n. 3, p. 488–493, 1979.

Heywood, N.; Cheng, D.-H. Comparison of methods for predicting head loss in turbulent pipe flow of non-newtonian fluids. **Transactions of the Institute of Measurement and Control**, v. 6, n. 1, p. 33–45, 1984.

Iceri, D. M.; Biazussi, J. L.; Geest, C. van der; Thompson, R. L.; Castro, M. S. de. Analysis of carbopol and triethanolamine concentration in the viscoplastic properties of aqueous solution. 2022.

Iceri, D. M.; Biazussi, J. L.; Geest, C. van der; Thompson, R. L.; Palermo, T.; Castro, M. S. The yielding behavior of aqueous solutions of carbopol and triethanolamine and its prediction considering the fractal nature of the formed aggregates. **Rheologica Acta**, p. 1–12, 2023.

Kelessidis, V. C.; Dalamarinis, P.; Maglione, R. Experimental study and predictions of pressure losses of fluids modeled as herschel–bulkley in concentric and eccentric annuli in laminar, transitional and turbulent flows. **Journal of Petroleum Science and Engineering**, v. 77, n. 3-4, p. 305–312, 2011.

Knaak, J.; Leung, H.-W.; Stott, W.; Busch, J.; Bilsky, J. Toxicology of mono-, di-, and triethanolamine. **Reviews of Environmental Contamination and Toxicology: Continuation of Residue Reviews**, p. 1–86, 1997.

Liu, Y.; Bruyn, J. R. de. Start-up flow of a yield-stress fluid in a vertical pipe. **Journal of Non-Newtonian Fluid Mechanics**, v. 257, p. 50–58, 2018.

Lubrizol. **Dispersion Techniques for Carbopol®* Polymers, Technical Report TDS-103**. [S.l.], 2007.

Lubrizol. **Molecular Weight of Carbopol®* and Pemulen®* Polymers, Technical Report TDS-222**. [S.l.], 2007.

Lubrizol. **Neutralizing Carbopol®* and Pemulen™* Polymers in Aqueous and Hydroalcoholic Systems, Technical Report TDS-237**. [S.l.], 2009.

Lubrizol. **Safety Data Sheet Carbopol® 940 NF Polymers**. [S.l.], 2022.

Lubrizol. **Carbopol® Polymer Products**. 2023. Disponível em: <https://www.lubrizol.com/Health/Pharmaceuticals/Excipients/Carbopol-Polymer-Products>.

Madlener, K.; Ciezki, H. Analytical description of the flow behavior of extended herschel-bulkley fluids with regard to gel propellants. **Energetic Materials-Performance und Safety**, p. 186–1, 2005.

Madlener, K.; Ciezki, H. Theoretical investigation of the flow behavior of gelled fuels of the extended herschel bulkley type. 2005.

Madlener, K.; Frey, B.; Ciezki, H. Generalized reynolds number for non-newtonian fluids. **Progress in propulsion physics**, v. 1, p. 237–250, 2009.

Magnon, E.; Cayeux, E. Precise method to estimate the herschel-bulkley parameters from pipe rheometer measurements. **Fluids**, v. 6, n. 4, p. 157, 2021.

Massey, B. Mechanics of fluids 4. th edition. **The English Language Book Society**, 1980.

Matoba, G. K.; Iceri, D. M.; Geest, C. van der; Thompson, R. L.; Castro, M. S. de. Cob-2023-1123 predicting friction factors in turbulent flow of herschel-bulkley fluids: A radial basis function neural network approach. 2023.

Metzner, A. Non-newtonian fluid flow. relationships between recent pressure-drop correlations. **Industrial & Engineering Chemistry**, v. 49, n. 9, p. 1429–1432, 1957.

Metzner, A.; Reed, J. Flow of non-newtonian fluids—correlation of the laminar, transition, and turbulent-flow regions. **Aiche journal**, v. 1, n. 4, p. 434–440, 1955.

Mooney, M. Explicit relations for slip. **J. Rheol**, v. 2, p. 210–221, 1931.

Oliveira, M. C. K. de; Teixeira, A.; Vieira, L. C.; Carvalho, R. M. de; Carvalho, A. B. M. de; Couto, B. C. do. Flow assurance study for waxy crude oils. **Energy & Fuels**, v. 26, n. 5, p. 2688–2695, 2012.

Ostertagova, E.; Ostertag, O. Forecasting using simple exponential smoothing method. **Acta Electrotechnica et Informatica**, v. 12, n. 3, p. 62, 2012.

Ostwald, W.; Auerbach, R. Ueber die viskosität kolloider lösungen im struktur-, laminar-und turbulenzgebiet: Ueber die geschwindigkeitsfunktion der viskosität disperser systeme, v. **Kolloid-Zeitschrift**, v. 38, p. 261–280, 1926.

Qi, P.; Honghai, F.; Haobo, Z.; Chaowei, L.; Xuyue, C.; Echuan, W.; Zhi, Y. General method of calculating annular laminar pressure drop of drilling fluids with different rheological models. **Petroleum Exploration and Development**, v. 40, n. 6, p. 806–810, 2013.

Rabinowitsch, B. Über die viskosität und elastizität von solen. **Zeitschrift für Physikalische Chemie**, v. 145A, n. 1, p. 1–26, 1929.

Rocha, N. O.; Khalil, C. N.; Leite, L. C.; Bastos, R. M. A thermochemical process for wax damage removal. In: SPE. **SPE International Conference on Oilfield Chemistry?** [S.l.], 2003. p. SPE–80266.

Rønningsen, H. P. Rheological behaviour of gelled, waxy north sea crude oils. **Journal of Petroleum Science and Engineering**, v. 7, n. 3-4, p. 177–213, 1992.

Saramito, P. **Complex fluids**. [S.l.]: Springer, 2016.

Sierra, A. G.; Varges, P. R.; Ribeiro, S. S. Startup flow of elasto-viscoplastic thixotropic materials in pipes. **Journal of Petroleum Science and Engineering**, v. 147, p. 427–434, 2016.

Slatter, P. T. Transitional and turbulent flow of non-newtonian slurries in pipes. 1995.

Swamee, P. K. Design of a submarine oil pipeline. **Journal of transportation Engineering**, v. 119, n. 1, p. 159–170, 1993.

Swamee, P. K.; Aggarwal, N. Explicit equations for laminar flow of herschel–bulkley fluids. **The Canadian Journal of Chemical Engineering**, v. 89, n. 6, p. 1426–1433, 2011.

Taghavi, S.; Alba, K.; Moyers-Gonzalez, M.; Frigaard, I. Incomplete fluid–fluid displacement of yield stress fluids in near-horizontal pipes: experiments and theory. **Journal of Non-Newtonian Fluid Mechanics**, v. 167, p. 59–74, 2012.

Tropea, C.; Yarin, A. L.; Foss, J. F. *et al.* **Springer handbook of experimental fluid mechanics**. [S.l.]: Springer, 2007. v. 1.

R. Varges, P.; M. Costa, C.; S. Fonseca, B.; F. Naccache, M.; Souza Mendes, P. R. de. Rheological characterization of carbopol® dispersions in water and in water/glycerol solutions. **Fluids**, v. 4, n. 1, p. 3, 2019.

White, F. **Mecânica dos Fluidos**. McGraw Hill Brasil, 2018. ISBN 9788580556070.

Xu, H.; Liao, S.-J. Laminar flow and heat transfer in the boundary-layer of non-newtonian fluids over a stretching flat sheet. **Computers & Mathematics with Applications**, v. 57, n. 9, p. 1425–1431, 2009.

Appendix

APPENDIX A – PRESSURE DROP GRADIENT VS. SHEAR STRESS RELATIONSHIP

To establish the relationship between the pressure drop gradient ($\Delta P/L$) and the shear stress (τ_{rz}) for a fluid flowing by pressure variation through a circular pipe, Chhabra e Richardson (2011) developed their analysis assuming the presence of a cylindrical volume portion of fluid with radius r located at the center of the pipe, as described in Figure A.1:

Figure A.1 – Cylindrical volume portion of fluid flowing through a tube (Chhabra; Richardson, 2011).

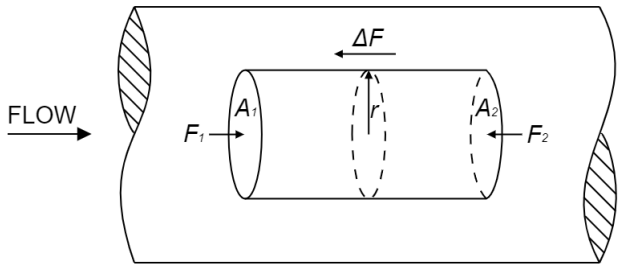

The balance of forces (F_1 and F_2) acting on the bases of the cylinder (A_1 and A_2), as shown in Figure A.1, is expressed by the Equation A.1:

$$F_1 - F_2 = \Delta F \tag{A.1}$$

By expressing the forces of Equation A.1 in terms of pressure (P) and area (A), and considering that the tangential force (ΔF) applied by the fluid on the surface of the pipe (A_{cylinder}) is the shear stress (τ_{rz}), as detailed in Equation 2.1 of Chapter 2 where $\tau_{rz} = F/A$, Equation A.1 can be reformulated as Equation A.2. This reformulation is graphically represented in Figure A.2:

Figure A.2 – Cylindrical element of radius r (Chhabra; Richardson, 2011).

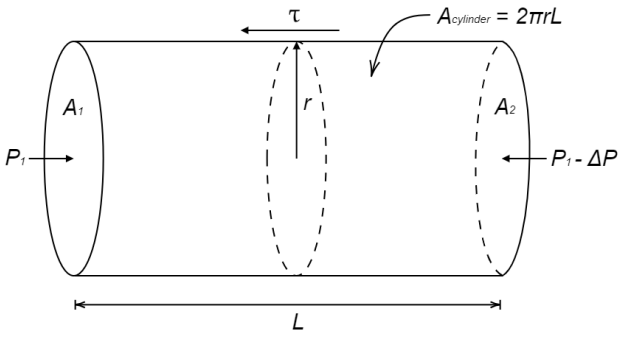

$$P_1 A_1 - (P_1 - \Delta P) A_2 = \tau_{rz} A_{\text{cylinder}}. \tag{A.2}$$

Rewriting area (A) as πr^2:

$$P_1(\pi r^2) - (P_1 - \Delta P)\pi r^2 = \tau_w(2\pi r L) \tag{A.3}$$

$$(\pi r) r (P_1 - P_1 + \Delta P) = \tau_{rz}\, 2(\pi r) L \tag{A.4}$$

$$\tau_{rz} = \left(\frac{\Delta P}{L}\right)\frac{r}{2} \tag{A.5}$$

The relationship demonstrates, as depicted in Figure A.3, a linear shear stress distribution profile across the cross section (variation of r) of the pipe. Therefore, in the axis of the pipe $(r = 0)$, the shear stress is 0.

Figure A.3 – Distribution of τ_{rz} in relation to r (Chhabra; Richardson, 2011).

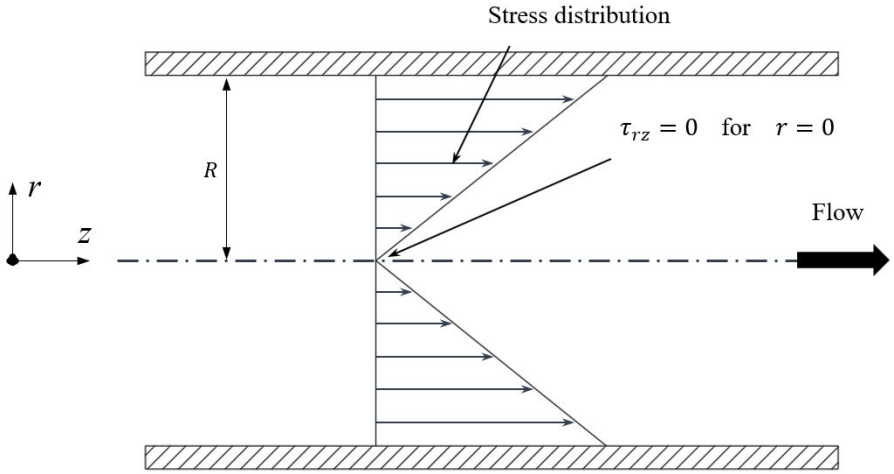

APPENDIX B – EQUATIONS FOR LAMINAR FLOW IN CIRCULAR SECTION PIPES APPLIED TO HERSCHEL-BULKLEY FLUIDS

In this appendix, the equations for the velocity distribution in laminar flow are presented, taking into account the presence of a solid plug-like core flowing through the center of a circular pipe, as well as the development of the equation for the volumetric flow rate applied to a Herschel-Bulkley fluid.

The Herschel-Bulkley fluid model in circular pipes is described by Equation 2.9, which, when expressed in polar coordinates, is given by:

$$\tau_{rz} = \tau_0^H + k\left(-\frac{\mathrm{d}V_z}{\mathrm{d}r}\right)^n \tag{B.1}$$

The relationship between pressure drop gradient and shear stress for an element of radius r relative to the coordinate origin (center of the pipe) developed by (Chhabra; Richardson, 2011) is given by:

$$\tau_{rz} = \left(-\frac{\Delta P}{L}\right)\frac{r}{2} \tag{B.2}$$

therefore,

$$\left(-\frac{\Delta P}{L}\right)\frac{r}{2} = \tau_0^H + k\left(-\frac{\mathrm{d}V_z}{\mathrm{d}r}\right)^n. \tag{B.3}$$

To find the equation that describes the velocity distribution within the pipe, it is necessary to integrate the Equation B.3 with respect to r:

$$\mathrm{d}V_z = -\left[\left(-\frac{\Delta P}{L}\right)\frac{r}{2k} - \frac{\tau_0^H}{k}\right]^{\frac{1}{n}}\mathrm{d}r$$

$$\int \mathrm{d}V_z = -\int\left[\left(-\frac{\Delta P}{L}\right)\frac{r}{2k} - \frac{\tau_0^H}{k}\right]^{\frac{1}{n}}\mathrm{d}r. \tag{B.4}$$

Before solving Equation B.4, a change of variables is made to facilitate the calculations:

$$a = \left(-\frac{\Delta P}{L}\right)\frac{1}{2k} \quad and \quad b = \frac{\tau_0^H}{k}$$

hence:

$$u = ar - b$$

$$\frac{\mathrm{d}}{\mathrm{d}u}u\mathrm{d}u = \frac{\mathrm{d}}{\mathrm{d}r}(ar - b)\mathrm{d}r$$

$$\mathrm{d}u = a\mathrm{d}r$$
$$\frac{\mathrm{d}u}{a} = \mathrm{d}r$$

and therefore, rearranging Equation B.4:

$$\int \mathrm{d}V_z = -\int u^{\frac{1}{n}} \frac{1}{a}\mathrm{d}u$$

$$V_z = -\frac{1}{a\left(\frac{1+n}{n}\right)} u^{(n+1)/n} + C = -\frac{a(ar-b)^{(n+1)/n}}{a(1+n)} + C$$

$$V_z = -\frac{n\left[\left(-\frac{\Delta P}{L}\right)\frac{r}{2k} - \frac{\tau_0^H}{k}\right]^{(n+1)/n}}{\left(-\frac{\Delta P}{L}\right)\frac{1}{2k}(1+n)} + C$$

$$V_z = -\left(-\frac{L}{\Delta P}\right) 2k \frac{n}{n+1}\left[\left(-\frac{\Delta P}{L}\right)\frac{r}{2k} - \frac{\tau_0^H}{k}\right]^{(n+1)/n} + C. \tag{B.5}$$

To ensure the physical relevance of Equation B.5, the no-slip condition at the wall, i.e. $V_z = 0$ when $r = R$, must be satisfied. Substituting the values for V_z and r in the last equation yields:

$$C = \left(-\frac{L}{\Delta P}\right) 2k \frac{n}{n+1}\left[\left(-\frac{\Delta P}{L}\right)\frac{R}{2k} - \frac{\tau_0^H}{k}\right]^{(n+1)/n} \tag{B.6}$$

$$\begin{aligned} V_z = \left(\frac{n}{n+1}\right)\Bigg[&-\left(-\frac{L}{\Delta P}\right) 2k \left(-\frac{\Delta P}{L}\frac{r}{2k} - \frac{\tau_0^H}{k}\right)^{(n+1)/n} \\ &+\left(-\frac{L}{\Delta P}\right) 2k \left(-\frac{\Delta P}{L}\frac{R}{2k} - \frac{\tau_0^H}{k}\right)^{(n+1)/n}\Bigg]. \end{aligned} \tag{B.7}$$

Conveniently, the mathematical artifice (R/R) is added to both terms of Equation B.7,

$$\begin{aligned} V_z = \left(\frac{n}{n+1}\right)\Bigg[&-\left(-\frac{L}{\Delta P}\right) 2k\frac{R}{R} \left(-\frac{\Delta P}{L}\frac{r}{2k} - \frac{\tau_0^H}{k}\right)^{(n+1)/n} \\ &+\left(-\frac{L}{\Delta P}\right) 2k\frac{R}{R} \left(-\frac{\Delta P}{L}\frac{R}{2k} - \frac{\tau_0^H}{k}\right)^{(n+1)/n}\Bigg] \end{aligned} \tag{B.8}$$

to introduce the definition of the wall shear stress described by Equation B.9 and thereby simplify the expression from Equation B.8:

$$\tau_w = \left(-\frac{\Delta P}{L}\right)\frac{R}{2} \tag{B.9}$$

$$\frac{\tau_0^H}{\tau_w} = \frac{R_p}{R} = \phi \tag{B.10}$$

$$V_z = \left(\frac{n}{n+1}\right)\left[-\frac{k}{\tau_w}R\left(\frac{\tau_w}{k}\frac{r}{R} - \frac{\tau_0^H}{k}\right)^{(n+1)/n} + \frac{k}{\tau_w}R\left(\frac{\tau_w}{k} - \frac{\tau_0^H}{k}\right)^{(n+1)/n}\right]$$

$$V_z = \left(\frac{nR}{n+1}\right)\left[\frac{k}{\tau_w}\left\{-\left(\frac{\tau_w}{k}\right)^{(n+1)/n}\left(\frac{r}{R} - \frac{\tau_0^H}{\tau_w}\right)^{(n+1)/n} + \left(\frac{\tau_w}{k}\right)^{(n+1)/n}\left(1 - \frac{\tau_0^H}{\tau_w}\right)^{(n+1)/n}\right\}\right].$$

By factoring out the common factors from the terms within the parentheses and substituting them into the last expression:

$$\begin{aligned} \tau_w^{-1} \quad . \quad \tau_w^{(n+1)/n} &= \tau_w^{1/n} \\ k \quad . \quad k^{-(n+1)/n} &= k^{-1/n} \end{aligned}$$

$$V_z = \left(\frac{nR}{n+1}\right)\left[-\tau_w^{1/n}k^{-1/n}\left\{\left(\frac{r}{R} - \phi\right)^{(n+1)/n}\right\} + \tau_w^{1/n}k^{-1/n}\left\{(1-\phi)^{(n+1)/n}\right\}\right]$$

$$V_z = \left(\frac{nR}{n+1}\right)\left[-\left(\frac{\tau_w}{k}\right)^{1/n}\left(\frac{r}{R} - \phi\right)^{(n+1)/n} + \left(\frac{\tau_w}{k}\right)^{1/n}(1-\phi)^{(n+1)/n}\right]$$

$$V_z = \left(\frac{nR}{n+1}\right)\left(\frac{\tau_w}{k}\right)^{1/n}\left[(1-\phi)^{(n+1)/n} - \left(\frac{r}{R} - \phi\right)^{(n+1)/n}\right] \tag{B.11}$$

Finally, Equation B.11 describes the velocity distribution within the pipe, nevertheless, it is only valid when $|\tau_{yx}|$ exceeds $\left|\tau_0^H\right|$, means, the region $R_p < r < R$. See the graphical representation of the regions in Figure 2.11 in Chapter 2. In order to determine the velocity distribution within the plug flow region $(0 \leq r \leq R_p)$, the substitution of $r = R_p$ is necessary, resulting in:

$$V_{zp} = \left(\frac{nR}{n+1}\right)\left(\frac{\tau_w}{k}\right)^{1/n}\left[(1-\phi)^{(n+1)/n} - \left(\frac{R_p}{R} - \phi\right)^{(n+1)/n}\right]$$

and simplifying the expression considering the relationship describe in Equation B.10, the velocity distribución inside the plug flow region is given by:

$$V_{zp} = \left(\frac{nR}{n+1}\right)\left(\frac{\tau_w}{k}\right)^{1/n}\left[(1-\phi)^{(n+1)/n}\right]. \tag{B.12}$$

Upon deriving the equations for the velocity distribution, the subsequent step involves the determination of the equation for the volumetric flow rate of the liquid:

$$\bar{V} = \frac{Q}{A}$$

$$Q = A \times \bar{V} = \int_0^R 2\pi r V_z \mathrm{d}r = \int_0^{R_p} 2\pi r V_{zp} \mathrm{d}r + \int_{R_p}^R 2\pi r V_z \mathrm{d}r. \tag{B.13}$$

Substituting the velocity distribution equations, V_z and V_{zp}, inside the Equation B.13:

$$\begin{aligned} Q = &\int_0^{R_p} (2\pi r) \frac{nR}{n+1} \left(\frac{\tau_w}{k}\right)^{1/n} \left[(1-\phi)^{(n+1)/n} \right] \mathrm{d}r \\ &+ \int_{R_p}^R (2\pi r) \frac{nR}{n+1} \left(\frac{\tau_w}{k}\right)^{1/n} \left[(1-\phi)^{(n+1)/n} - \left(\frac{r}{R} - \phi\right)^{(n+1)/n} \right] \mathrm{d}r. \end{aligned} \tag{B.14}$$

The definite integral B.14 is resolved by terms resulting in:

for the first term:

$$\begin{aligned} Q_1 &= \int_0^{R_p} (2\pi r) \frac{nR}{n+1} \left(\frac{\tau_w}{k}\right)^{1/n} \left[(1-\phi)^{(n+1)/n} \right] \mathrm{d}r \\ Q_1 &= (2\pi) \frac{nR}{n+1} \left(\frac{\tau_w}{k}\right)^{1/n} \left[(1-\phi)^{(n+1)/n} \right] \int_0^{R_p} r \mathrm{d}r \\ Q_1 &= (2\pi) \frac{nR}{n+1} \left(\frac{\tau_w}{k}\right)^{1/n} \left[(1-\phi)^{(n+1)/n} \right] \left. \frac{r^2}{2} \right|_0^{R_p} \\ Q_1 &= (\pi) \frac{nR}{n+1} \left(\frac{\tau_w}{k}\right)^{1/n} \left[(1-\phi)^{(n+1)/n} \right] R_p^2 \frac{R^2}{R^2} \\ Q_1 &= \frac{\pi n R^3}{n+1} \left(\frac{\tau_w}{k}\right)^{1/n} \left[(1-\phi)^{(n+1)/n} \right] \phi^2. \end{aligned} \tag{B.15}$$

and, for the second term:

$$\begin{aligned} Q_2 &= \int_{R_p}^R (2\pi r) \frac{nR}{n+1} \left(\frac{\tau_w}{k}\right)^{1/n} \left[(1-\phi)^{(n+1)/n} - \left(\frac{r}{R} - \phi\right)^{(n+1)/n} \right] \mathrm{d}r \\ Q_2 &= \int_{R_p}^R (2\pi r) \frac{nR}{n+1} \left(\frac{\tau_w}{k}\right)^{1/n} (1-\phi)^{(n+1)/n} \mathrm{d}r \\ &\quad - \int_{R_p}^R (2\pi r) \frac{nR}{n+1} \left(\frac{\tau_w}{k}\right)^{1/n} \left(\frac{r}{R} - \phi\right)^{(n+1)/n} \mathrm{d}r \end{aligned} \tag{B.16}$$

Now, by solving the first term of Equation B.16, which subsequently becomes the third term of Equation B.14:

$$\begin{aligned} Q_3 &= \int_{R_p}^R (2\pi r) \frac{nR}{n+1} \left(\frac{\tau_w}{k}\right)^{1/n} (1-\phi)^{(n+1)/n} \mathrm{d}r \\ Q_3 &= (2\pi) \frac{nR}{n+1} \left(\frac{\tau_w}{k}\right)^{1/n} (1-\phi)^{(n+1)/n} \int_{R_p}^R r \, \mathrm{d}r \end{aligned}$$

$$Q_3 = (2\pi) \frac{nR}{n+1} \left(\frac{\tau_w}{k}\right)^{1/n} (1-\phi)^{(n+1)/n} \left. \frac{r^2}{2} \right|_0^{R_p} = (\pi) \frac{nR}{n+1} \left(\frac{\tau_w}{k}\right)^{1/n} (1-\phi)^{(n+1)/n} \left(R^2 - R_p^2\right)$$

$$Q_3 = (\pi)\,\frac{nR}{n+1}\left(\frac{\tau_w}{k}\right)^{1/n}(1-\phi)^{(n+1)/n}\,R^2\left(1-\frac{R_p^2}{R^2}\right)$$

$$Q_3 = \frac{\pi n R^3}{n+1}\left(\frac{\tau_w}{k}\right)^{1/n}\left[(1-\phi)^{(n+1)/n}\right]\left(1-\phi^2\right) \tag{B.17}$$

and, finally, the last term of Equation B.16, now the fourth term of Equation B.14:

$$Q_4 = \int_{R_p}^{R}(2\pi r)\,\frac{nR}{n+1}\left(\frac{\tau_w}{k}\right)^{1/n}\left(\frac{r}{R}-\phi\right)^{(n+1)/n}\mathrm{d}r$$

$$Q_4 = (2\pi)\,\frac{nR}{n+1}\left(\frac{\tau_w}{k}\right)^{1/n}\int_{R_p}^{R} r\left(\frac{r}{R}-\phi\right)^{(n+1)/n}\mathrm{d}r.$$

Some substitutions and variable changes can be applied to facilitate the resolution of Q_4:

$$\psi = (2\pi)\,\frac{nR}{n+1}\left(\frac{\tau_w}{k}\right)^{1/n}$$

$$a = \frac{1}{R} \quad and \quad b = \phi$$

and, deriving variable changes:

$$u = ar - b$$

$$\frac{\mathrm{d}}{\mathrm{d}u}u\mathrm{d}u = \frac{\mathrm{d}}{\mathrm{d}r}(ar-b)\mathrm{d}r$$

$$\mathrm{d}u = a\mathrm{d}r$$

$$\frac{\mathrm{d}u}{a} = \mathrm{d}r.$$

Reorganizing Q_4 and taking into account the ratio $(R_p/R) = \phi$ from Equation B.10,

$$Q_4 = \psi\int_{R_p}^{R} R.R\,(u-\phi)\,u^{(n+1)/n}\mathrm{d}u = \psi R^2\int_{R_p}^{R}u^{(2n+1)/n}\mathrm{d}u + \psi\phi R^2\int_{R_p}^{R}u^{(n+1)/n}\mathrm{d}u$$

$$Q_4 = \psi R^2\ \left(\frac{nu^{(3n+1)/n}}{3n+1}\right)\Bigg|_{R_p}^{R} + \psi\phi R^2\ \left(\frac{nu^{(2n+1)/n}}{2n+1}\right)\Bigg|_{R_p}^{R}$$

$$Q_4 = \psi R^2\ \left[\frac{n\left(\frac{r}{R}-\phi\right)^{(3n+1)/n}}{3n+1}\right]\Bigg|_{R_p}^{R} + \psi\phi R^2\ \left[\frac{n\left(\frac{r}{R}-\phi\right)^{(2n+1)/n}}{2n+1}\right]\Bigg|_{R_p}^{R}$$

$$Q_4 = \psi R^2\left[\frac{n\,(1-\phi)^{(3n+1)/n}}{3n+1}\right] + \psi\phi R^2\left[\frac{n\,(1-\phi)^{(2n+1)/n}}{2n+1}\right]$$

$$Q_4 = \frac{\pi n R^3}{n+1}\left(\frac{\tau_w}{k}\right)^{1/n}\left[(1-\phi)^{(n+1)/n}\right] \times \left[\frac{2n\,(1-\phi)^2}{(3n+1)} + \frac{2n\phi\,(1-\phi)}{2n+1}\right]. \tag{B.18}$$

And finally, by combining equations B.15, B.17, and B.18, which were derived from the integration of Equation B.14, can be rearranged to obtain the final expression to calculate the volumetric flow rate of the liquid in circular section pipes under laminar regime flow conditions, considering the impact of Herschel-Bulkley fluids:

$$Q = Q_1 + Q_3 - Q_4$$

$$Q = \frac{\pi n R^3}{n+1}\left(\frac{\tau_w}{k}\right)^{1/n}\left[(1-\phi)^{(n+1)/n}\right] \times \left[\phi^2 + 1 - \phi^2 - \frac{2n\,(1-\phi)^2}{(3n+1)} - \frac{2n\phi\,(1-\phi)}{2n+1}\right]$$

$$Q = \pi n R^3\left(\frac{\tau_w}{k}\right)^{1/n}\left[(1-\phi)^{(n+1)/n}\right] \times \left[\frac{2n}{n+1}\left(\frac{1}{2n} - \frac{(1-\phi)^2}{(3n+1)} - \frac{\phi\,(1-\phi)}{2n+1}\right)\right] \tag{B.19}$$

APPENDIX C – VALIDATION OF THE EXPERIMENTAL APPARATUS

Two experiments were conducted to analyze the pressure drop of water, a well-known Newtonian fluid, in single-phase flow. As detailed in Tables C.1 and C.2, both tests covered different velocity ranges, Reynolds numbers, and pressure drops to validate the sensors installed in the experimental apparatus under various flow operating conditions. Test 1 evaluated the performance of the sensors in flow regimes with slower transitions, characterized by lower Reynolds numbers and pressure drops. In contrast, Test 2 focused on highly turbulent flows with higher Reynolds numbers and greater pressure drops. The experimental results from both tests were compared with theoretical predictions obtained through the Colebrook-White correlation (Equation C.1) and the Fanning equation (Equation C.2), allowing for verification of the measurement accuracy:

$$\frac{1}{\sqrt{f}} = -4log\left(\frac{\varepsilon/D}{3.7} + \frac{2.51}{N_{\text{Re}}\sqrt{4f}}\right) \tag{C.1}$$

$$\Delta P = \frac{2fL\rho V^2}{D}. \tag{C.2}$$

Table C.1 – Test 1 - Water single-phase flow test for validation of the experimental apparatus.

V **(m/s)**	N_{Re} **(-)**	f_{exp} **(-)**	ΔP_{exp}**(Pa)**	f **(-) Colebrook**	ΔP_{c}**(Pa)**	T_{in} **(°C)**	T_{out} **(°C)**
0.0294	1 556	0.0091	1	0.0103	1	28.5	28.7
0.0509	2 694	0.0332	8	0.0118	3	27.1	27.2
0.0686	3 631	0.0201	9	0.0109	5	26.6	26.7
0.0871	4 611	0.0164	11	0.0103	7	26.2	26.2
0.1783	9 433	0.0111	32	0.0088	25	25.9	26.0
0.4072	21 540	0.0081	122	0.0077	116	30.3	30.5
0.5875	31 076	0.0074	232	0.0075	230	30.8	30.9
0.7652	40 473	0.0071	375	0.0072	381	31.2	31.3
0.9444	49 956	0.0068	551	0.0071	570	31.7	31.9
1.0887	57 055	0.0067	705	0.0070	736	32.1	32.2

Table C.2 – Test 2 - Water single-phase flow test for validation of the experimental apparatus.

V **(m/s)**	$N_{\mathbf{Re}}$ **(-)**	$f_{\mathbf{exp}}$ **(-)**	$\Delta P_{\mathbf{exp}}$**(Pa)**	f **(-) Colebrook**	$\Delta P_{\mathbf{c}}$**(Pa)**	$T_{\mathbf{in}}$ **(°C)**	$T_{\mathbf{out}}$ **(°C)**
0.8159	43 157	0.0088	531	0.0072	427	25.6	25.7
1.0000	52 841	0.0079	713	0.0070	631	25.7	25.8
1.2712	67 240	0.0072	1 055	0.0069	1 016	25.8	25.9
1.5352	81 309	0.0069	1 465	0.0068	1 461	25.8	25.9

Figures C.1 and C.2 show the measured pressure drop (ΔP_{exp}) and the theoretical pressure drop curve (ΔP_{c}) calculated with the Colebrook-White correlation. The experimental results are consistent, as they follow the Colebrook-White trend, and the calculated values are within or very close to the vertical bar representing the sensor's precision, equivalent to 60 Pa. The performance indicators for Test 1 show a mean absolute error (MAE) of 8.33 Pa and a mean absolute percentage error (MAPE) of $19.70\,\%$. For Test 2, the MAE is 57.85 Pa, and the MAPE is $8.81\,\%$:

Figure C.1 – Comparison of experimental pressure drop vs. theoretical curve calculated by Colebrook-White.

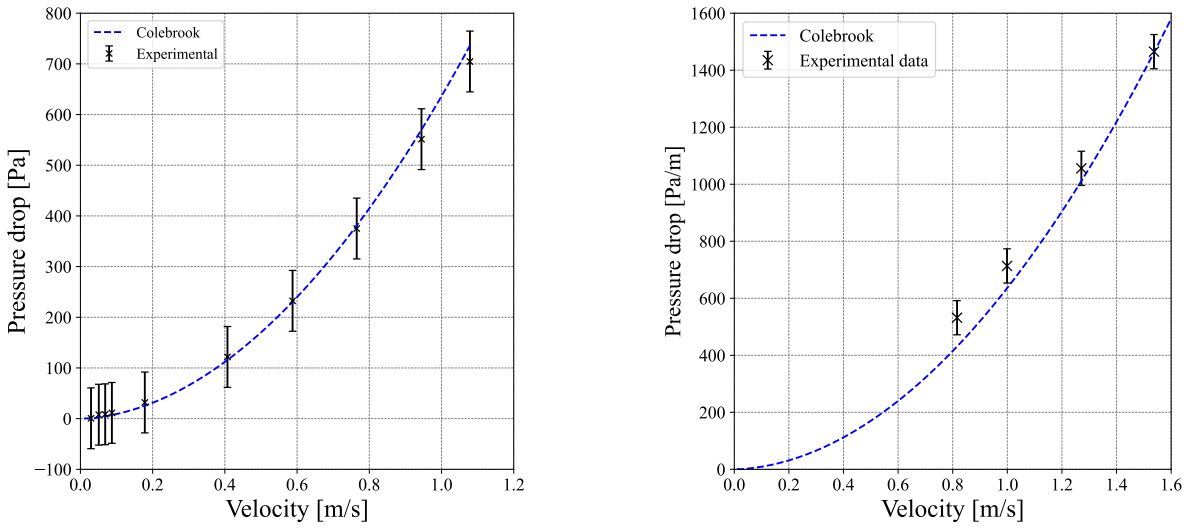

(a) Test 1

(b) Test 2

Figure C.2 – Pressure drop comparison for single-phase flow test.

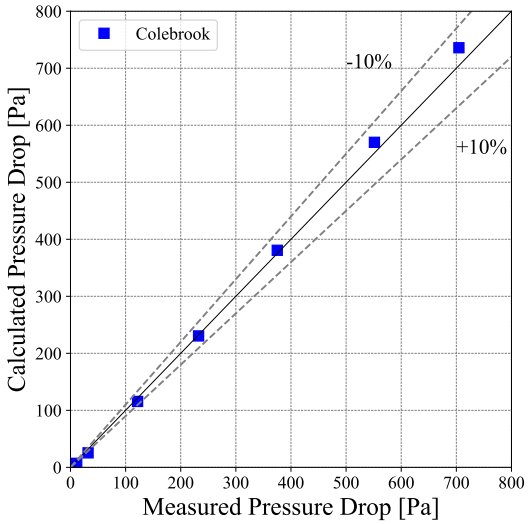

(a) Test 1

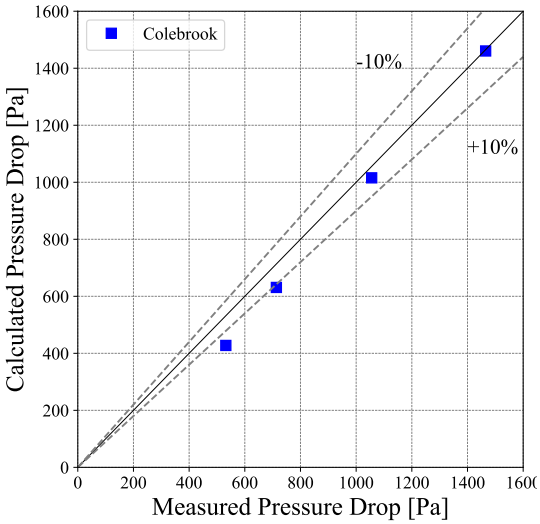

(b) Test 2

These measurements not only validate the experimental apparatus but also ensure data consistency, thereby enhancing confidence in the quality of the experimental results obtained using the Herschel-Bulkley fluid.

APPENDIX D – EXPERIMENTAL DATA FROM GÜZEL

Table D.1 – Experimental measurements of Güzel *et al.* (2009a) study for fluid 1.

V **(m/s)**	$\Delta P_{\mathbf{exp}}/\rho g L$	τ_0^H **(Pa)**	k **(Pa.s^n)**	n **(-)**	R_p **(mm)**	T **(°C)**
0.1278	0.19557	6.0	4.79	0.37	6.29	31
1.068	0.3490	5.7	3.66	0.42	3.33	32
1.304	0.36577	5.7	3.28	0.44	3.11	32
2.5573	0.43450	5.6	2.87	0.46	2.40	35

Table D.2 – Experimental measurements of Güzel *et al.* (2009a) study for fluid 2.

V **(m/s)**	$\Delta P_{\mathbf{exp}}/\rho g L$	τ_0^H **(Pa)**	k **(Pa.s^n)**	n **(-)**	R_p **(mm)**	T **(°C)**
0.3039	0.08942	1.80	1.11	0.50	4.11	34
1.0233	0.12817	1.58	0.71	0.53	2.90	34
1.5457	0.14526	0.95	0.60	0.54	1.67	34.5

Table D.3 – Experimental measurements of Güzel *et al.* (2009a) study for fluid 3.

V **(m/s)**	$\Delta P_{\mathbf{exp}}/\rho g L$	τ_0^H **(Pa)**	k **(Pa.s^n)**	n **(-)**	R_p **(mm)**	T **(°C)**
0.11202	0.08399	2.0	2.05	0.36	5.55	29
0.4622	0.13224	1.5	2.01	0.40	2.57	29
1.2076	0.17804	1.4	1.59	0.43	1.84	29
2.0461	0.22166	1.3	1.20	0.48	1.40	31
2.3218	0.23598	1.2	0.92	0.53	1.20	32.5

Table D.4 – Experimental measurements of Güzel *et al.* (2009a) study for fluid 4.

V **(m/s)**	$\Delta P_{\mathbf{exp}}/\rho g L$	τ_0^H	k **(Pa.s^n)**	n **(-)**	R_p **(mm)**	T **(°C)**
0.3902	0.04421	0.38	0.37	0.58	1.89	30
0.7227	0.05769	0.30	0.29	0.60	1.29	30
1.0754	0.06961	0.28	0.26	0.61	1.01	30